Performance Analysis and Operating Limits of Dual Inverter Open Winding IPMSM Drives

by

Gayan Madusanka Amaradasa Watthewaduge

A thesis submitted to the Faculty of Graduate Studies of
The University of Manitoba
in partial fulfilment of the requirements for the degree of

MASTER OF SCIENCE

Department of Electrical and Computer Engineering
University of Manitoba
Winnipeg.

Abstract

Operating capabilities of a dual inverter Open Winding Interior Permanent Magnet Synchronous Motor drive are investigated and compared with those of a conventional single inverter drive in Maximum Torque per Ampere and Field Weakening regions. To predict the performance and operating limits of the drive systems with improved accuracy, the impact of saturation on inductances and Permanent Magnet flux linkage values are taken into account, and core, copper, friction and windage, and solid losses (due to skin and proximity effects and magnet losses) are considered in a wide speed range. It is shown how core saturation affects the d- and q-axis inductances and saliency ratio, and electromagnetic and mechanical losses significantly change in various operating points. It is revealed how the above effects may affect the operating capability of the machine in different drive configurations. Different active and reactive power sharing assumptions are made in the dual inverter drives, and it is shown how each of the related controllers is accordingly defined. It is demonstrated that in certain operating regions of the open winding machine's torque versus speed envelope, the original active and reactive power sharing principles and the defined controllers have to be modified, otherwise the machine may not be able to operate throughout its entire anticipated operating points. Performance prediction is conducted using machine's electromagnetic parameters and losses that are obtained via Finite Element Analysis, coupled with an optimization algorithm to find optimal operating points in Maximum Torque Per Ampere and Field Weakening regions. The analytical findings are further validated against experimental results obtained from a 1-kW dual inverter Interior Permanent Magnet Synchronous motor drive.

Copyright Forms

I would like to acknowledge the use of the following IEEE papers in preparation of this thesis.

Acknowledgement

This thesis becomes successful with the support of many individuals. I would like to convey my sincere appreciation to all of them.

First, I would like to express my sincere gratitude to my advisor, Prof. Shaahin Filizadeh for his continuous guidance and consistent advice throughout the research. I have learnt valuable lessons for my life from his wisdom, vision, and hard working.

I would like to especially thank Dr. Mohammad Sedigh Toulabi for his valuable time, effort, consistence guidance and knowledge sharing during this research.

I would like to extend the special thank you to my examining committee members, Dr. Udaya Annakkage and Dr. Matt Khoshdarregi for taking time to review my thesis.

I would also like to acknowledge the support given by academic and non-academic staff of the Department of Electrical and Computer Engineering, all the colleagues and friends. Furthermore, I am grateful to the Faculty of Graduate Studies, University of Manitoba and Natural Science and Engineering Research Council (NSERC) of Canada for providing financial support for the research.

Last but not least, I would like to pay acknowledgement to each and every one, who shared their knowledge and experience in the process of accomplishing this endeavour.

In dedication to

My Wife and My Parents,

All My Teachers

And Friends

Table of Contents

Chapter 3- Effects of Saturation and Losses on the Predicted Performance of an IPMSM

Chapter 4- Dual Inverter Open Winding Drives

Chapter 5- Experimental Verification

List of Tables

List of Figures

Abbreviations

AC	Alternative Current
BEMF	Back Electromotive Force
BLDC	Brushless DC Motor
CCCP	Constant Current Constant Power Control
CMV	Common Mode Voltage
CPR	Cycles per Revolution
CVCPC	Constant Voltage Constant Power Control
DC	Direct Current
DTC	Direct Torque Control
EV	Electric Vehicle
FEA	Finite Element Analysis
FFT	Fast Fourier Transform
FOC	Field Oriented Control
FW	Field Weakening
HEV	Hybrid Electric Vehicle
IDID	Isolated Dual Inverter Drive
IPMSM	Interior Permanent Magnet Synchronous Motor
KVL	Kirchhoff's Voltage Law
MMC	Modular Multilevel Converter
MMF	Magneto Motive Force

MTPA	Maximum Torque per Ampere
MV	Medium Voltage
NDID	Non-Isolated Dual Inverter Drive
OCV	Optimal Current Voltage
OF	Objective Function
OW	Open Winding
PM	Permanent Magnet
PMSM	Permanent Magnet Synchronous Machine
PWM	Pulse Width Modulation
RTDS	Real Time Digital Simulator
SPMSM	Surface Permanent Magnet Synchronous Motor
SPWM	Sinusoidal Pulse Width Modulation
SVM	Space Vector Modulation
V2G	Vehicle to Grid
VCLMT	Voltage Current Limited Maximum Torque
VSC	Voltage Source Converter
VSD	Variable Speed Drive

Nomenclature

a, b, x	Steinmetz Coefficients	
B_p	Peak flux density	(Wb/m^2)
f_e	Electrical frequency	(Hz)
i_a, i_b, i_c	Three phase currents of the machine	(A)
i_d, i_q	d- and q-axis currents	(A)
$i_{d,ref}$, $i_{q,ref}$	d- and q-axis reference currents	(A)
i_{dF}, i_{qF}	Filtered d- and q-axis reference currents	(A)
I_{max}	Maximum peak stator current	(A)
i_{peak}	Peak stator current	(A)
L_{aa}, L_{bb}, L_{cc}	Self-inductance of three phases	(H)
L_{ab}, L_{ac}	Mutual inductance of Phase-a and Phase-b, Phase-c	(H)
L_{ba}, L_{bc}	Mutual inductance of Phase-b and Phase-a, Phase-c	(H)
L_{cb}, L_{ca}	Mutual inductance of Phase-c and Phase-b, Phase-a	(H)
L_d, L_q	d- and q-axis inductances	(H)
p	Number of poles	
P_1	Input active power of the VSC-1	(W)
P_2	Input active power of the VSC-2	(W)
P_{core}	Core losses	(W)
P_{cu}	Copper losses	(W)
P_{eddy}	Eddy current losses	(W)
P_{hys}	Hysteresis losses	(W)
P_m,	Input active power of the machine	(W)

P_{mech}	Mechanical losses	(W)
P_{out}	Output mechanical power of the machine	(W)
P_{solid}	Solid losses	(W)
P_{stray}	Stray losses	(W)
R_s	Per phase stator DC resistance	(Ω)
T_{dev}	Developed mechanical torque	(Nm)
T_e	Electromagnetic torque	(Nm)
v_1, v_2	VSC-1 and VSC-2 phase voltage	(V)
v_{1a}, v_{1b}, v_{1c}	Three phase terminal voltages of VSC-1	(V)
v_{1d}, v_{1q}	d- and q-axis voltage components of VSC-1	(V)
v_{1LL}, v_{2LL}	Line to line voltage of VSC-1 and VSC-2	(V)
v_{2a}, v_{2b}, v_{2c}	Three phase terminal voltages of VSC-2	(V)
v_{2d}, v_{2q}	d- and q-axis voltage components of VSC-2	(V)
v_a, v_b, v_c	Three phase stator terminal voltages	(V)
v_{cap}	Capacitor voltage of VSC-2	(V)
$v_{cap,ref}$	Reference capacitor voltage of VSC-2	(V)
V_{DC}	DC link voltage	(V)
v_m	Machine's phase voltage	(V)
V_{max}	Maximum peak stator voltage	(V)
v_{md}, v_{mq}	d- and q-axis voltage components of machine	(V)
X_a, X_b, X_c	Three phase time domain variable quantities	
X_d, X_q, X_0	dq0 variable quantities	
β	Current angle	(degree)

θ_r	Rotor position (electrical angle)	(rad)
λ_a, λ_b, λ_c	Three phase flux linkages of stator	(Wb)
λ_d, λ_q	d- and q-axis flux linkage components	(Wb)
λ_{pm}	Peak per phase flux linkage due to permanent magnets	(Wb)
λ_{pma}, λ_{pmb}, λ_{pmc}	Three phase flux linkages of stator due to permanent magnets	(Wb)
ω_e	Electrical angular speed	(rad/s)
$\omega_{e,ref}$	Reference electrical angular speed	(rad/s)
ω_m	Mechanical angular speed	(rad/s)

Chapter 1

Introduction

1.1 Background, Challenges, and Motivations

In recent decades, Permanent Magnet Synchronous Machines (PMSMs) have always been one of the most attractive machines in electromechanical energy conversion systems. PMSMs are widely used in industrial applications including wind energy conversion systems [1] and Electric Vehicle (EV) propulsion systems [2], due to their high efficiency, high torque density, large power factor, low maintenance requirement, and wide Field Weakening (FW) capability [3-5].

Open Winding (OW) motor drive systems have received noticeable attention in the recent years as a replacement alternative for conventional motor drive systems. An OW machine does not have a neutral point and the phase leads of the machine can be fed by two separate Voltage Source Converters (VSCs). These VSCs may support the active and/or reactive power demands of the machine in various operating points. OW motor drive systems are popular in various applications such as EV propulsion systems [6], Medium Voltage (MV) Motor Drive systems, which uses Modular Multi-Level Converters (MMC) [7], and wind energy generation systems [8].

The performance capabilities of an Interior Permanent Magnet Synchronous Machine (IPMSM) in both conventional and dual inverter OW motor drive systems are directly a function of the magnetic saturation in its stator and rotor cores [9-11] as well as the associated electromagnetic and mechanical losses [12-13]. The performance prediction may not be accurate unless behaviour of the magnetic field distribution in stator/rotor core are fully taken into account. Since the electromagnetic losses and mechanical losses are significant at higher speeds, those loss

components are also required to be accurately considered in the analysis to obtain a better prediction of machine's capabilities.

According to the application requirements, different strategies have been introduced in literature for speed control of PMSMs [14]. Typically, an IPMSM is driven to provide a constant torque up to its base speed, i.e., constant torque or Maximum Torque Per Ampere (MTPA) region. After the base speed, the torque produced by the IPMSM is inversely proportional to the speed up to its maximum speed while this operating region is called FW region. The ideal operating characteristic of the IPMSM in a wide speed range is shown in Figure 1.1. In most industrial applications, the MTPA control technique and Voltage Current Limited Maximum Torque Control (VCLMT) technique are commonly used to control the machine in constant torque and field weakening regions, respectively [15].

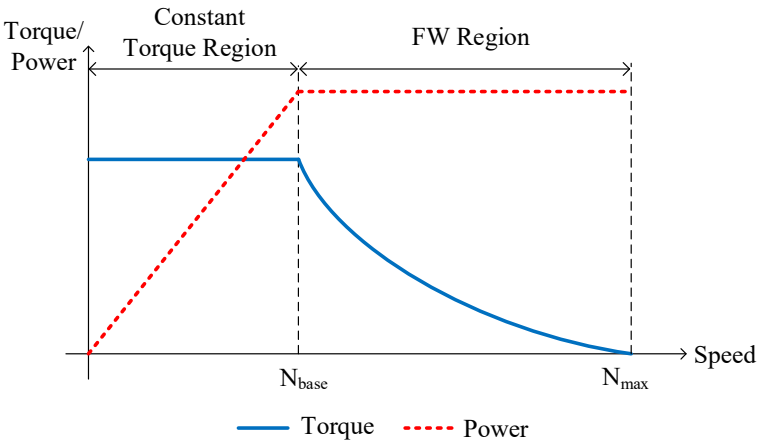

Figure 1.1 Torque/Power versus speed characteristics

As the main motivation of this thesis, the performance capability of an IPMSM including its torque and power potentials are predicted considering the effects of core saturation and losses of the machine for both conventional single inverter and dual inverter OW drives. The saturation and losses are analysed using a Finite Element model of the machine and the performance capabilities

of the machine are predicted in a wide speed range in both MTPA and FW regions. To verify the simulation expectations, experimental evaluations are also conducted in a wide speed range.

1.2 Thesis Outline

Chapter 2 presents the classification of Permanent Magnet (PM) machines, the structure of stator and rotor of PMSMs, the basic equations of the machine in both time domain and d-q reference frame, and the fundamentals of Field Oriented Control (FOC) theory for PMSMs using MTPA and VCLMT control techniques.

Chapter 3 shows how the core saturation significantly affects the inductances, PM flux linkage, and electromagnetic losses during machine's loading and wide operational speeds. It also introduces the modified steady state d-q domain equations for the developed torque of the machine taking into account the machine's losses. It is shown how MTPA and VCLMT control algorithms have to be fulfilled taking into account all non-linearities and associated losses. The control considerations for the conventional single inverter drive are presented including its corresponding control block diagram. This chapter validates the importance of considering the nonlinearities and losses for predicting the output power, maximum torque capability, and d-axis reference current trajectory in a wide speed range.

Chapter 4 introduces the dual inverter OW IPMSM drives. It discusses about three dual inverter drive control strategies based on different defined active and reactive power sharing assumptions between two utilized VSCs. Corresponding control block diagrams for the considered dual inverter drives are separately introduced, and the predicted performance capabilities of each drive structure is compared with a conventional single inverter drive in both MTPA and FW regions.

Chapter 5 shows the prepared test ring and experimental results for all single and dual inverter drive systems. The experimental performance capabilities of the IPMSM are compared with the simulation analysis and the minor observed discrepancies are highlighted and discussed in further details.

Chapter 6 describes the contribution of the thesis and deals with the concluding remarks. Recommendations for future work and suggestions for improving the contributions of the thesis research are briefly discussed as well.

Chapter 2

Literature Review: Wide Speed Range Operation and Control of PMSMs

In this chapter, classification of PM machines and different rotor geometries of PMSMs are introduced. The voltage and flux linkage equations are developed in time domain using Kirchhoff and Faraday laws. Using the rotating reference frame theory, the developed torque of an IPMSM is introduced in d-q frame. The concept of MTPA and VCLMT control techniques are investigated for IPM machines under ideal operating conditions neglecting the saturation and losses effects. The mathematical equations for the ideal d-axis reference current are extracted for both control techniques and the control diagram of a conventional single inverter IPMSM drive is introduced at the end of the chapter.

2.1 Structure of a PMSM

PM machines can be mainly classified into two categories, i.e., Alternative Current (AC) machines and Direct Current (DC) machines. There are two types of PM AC machines based on the shape of the induced Back Electromotive Force (BEMF). The shape of the BEMF of a Brushless DC (BLDC) machine is trapezoidal, where as that of a PMSM is sinusoidal because of the specific winding pattern of each case. Moreover, there are two different types of PMSMs as categorized in Figure 2.1. These two types are Surface Permanent Magnet Synchronous Machines (SPMSM) whose PMs are mounted on the rotor surface, and IPMSMs whose PMs are buried inside the rotor. The rotor geometry of a SPMSM is illustrated in Figure 2.2.

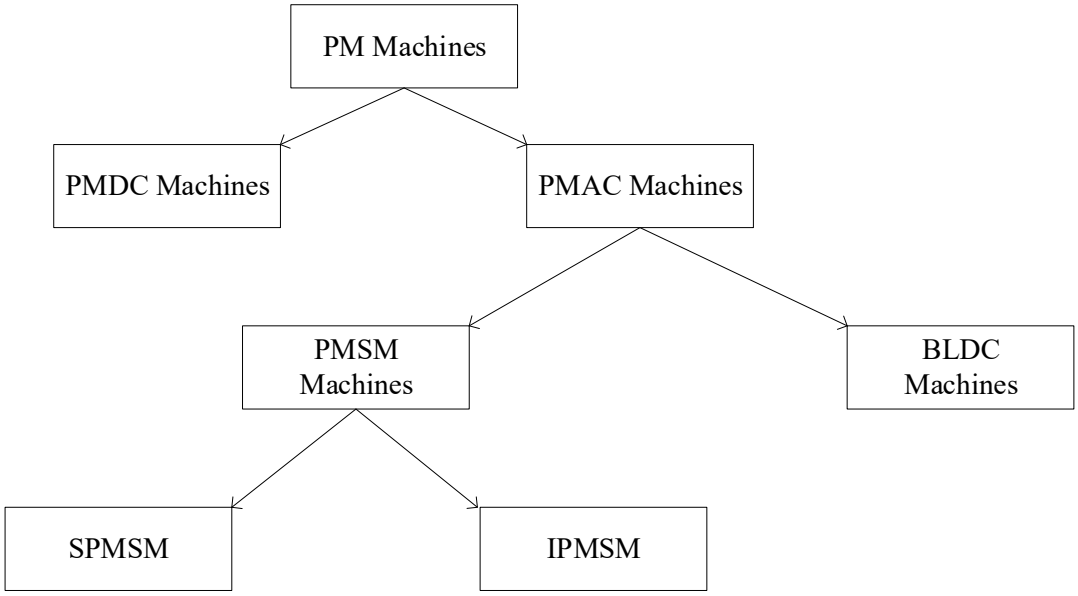

Figure 2.1 Classification of PM machines

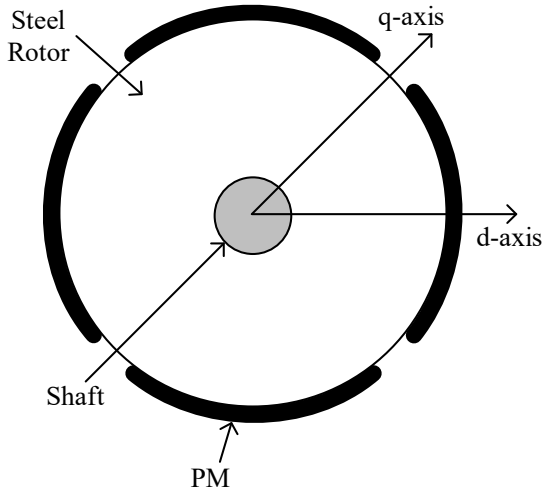

Figure 2.2 Rotor geometry of a SPMSM

The inductance of SPMSM does not vary with the rotor position, which means the d-axis and q-axis inductances (L_d, and L_q) and reluctances are the same for SPMSMs. However, since the PMs are located inside the rotor of IPMSM, the equivalent reluctance value through the air gap along the rotor PMs to stator is larger than that of along the steel to the stator. That is why L_d is smaller than L_q in an IPMSM, which introduces a saliency ratio (L_q/L_d) value larger than unity in

this type of machine. As a result, IPMSM can provide an additional reluctance torque component to the existing electromagnetic torque. The flux paths along the d- and q-axes in an IPMSM are shown in Figure 2.3.

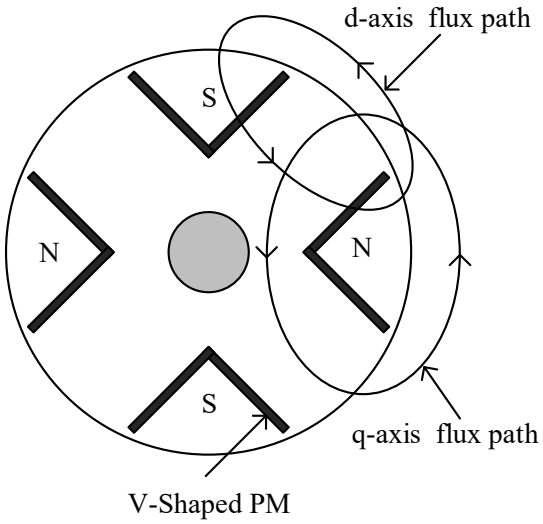

Figure 2.3 Flux paths in an IPMSM

The IPMSM has several key advantages over SPMSM including (i) the buried magnet rotor structure helps to operate the IPMSM at a wider speed range due to its higher structural strength, (ii) the additional reluctance torque component due to a salient rotor structure is useful in FW operation and increases the torque density of the IPMSM, and (iii) by adjusting the rotor geometry, the saliency ratio of an IPMSM can be specified in a way to better match the design's desired requirements [16].

There are different rotor geometries for IPMSMs based on the PM arrangement (i) Spoke type, (ii) Tangential type, (iii) V-shaped, and (iv) U-shaped. These rotor types are illustrated in Figure 2.4.

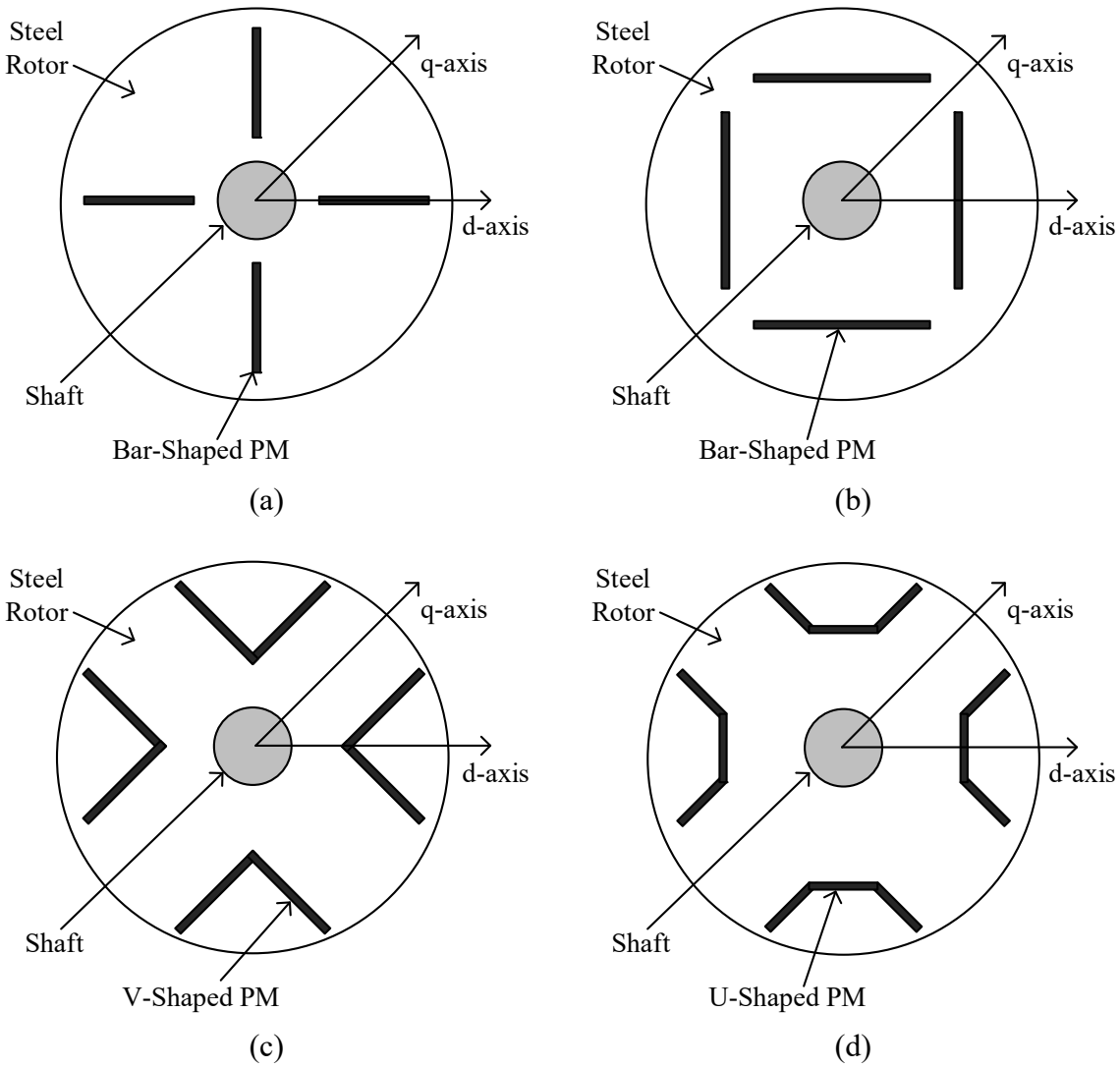

Figure 2.4 Rotor geometries of IPMSMs: (a) Spoke type, (b) Tangential type, (c) V-shaped and (d) U-shaped.

In this thesis, a V-shaped PMSM is used since it has a higher flux concentration [17] and a better electromagnetic performance in terms of average torque, reluctance torque, power density, and power factor [18].

2.2 Theory of Operation

In general, the stator of a three-phase PMSM is cylindrical and constructed with three-phase balanced AC windings, which are excited with a three-phase voltage source that creates a rotating

magnetic field distributed inside the air gap; the rotor's PMs start to follow this rotating magnetic field.

The stator winding structure of an AC machine determines the Magnetomotive Force (MMF) distribution in the air gap. The harmonic contents of machine are highly affected by the MMF distribution causing the losses of machine to significantly change. Depending on the winding layout structure and consequently MMF distribution, there are two main winding configurations for an AC machine, i.e., concentrated winding and distributed winding.

In a concentrated winding, the winding coils are usually concentrated at stator slots and the opposite end of each winding is located at next stator slot. A concentrated winding offers inherent advantages such as reduction of the copper volume of the winding (indirectly reduces the copper losses), construction simplicity, and reduction of the effective axial length of the machine [19]. However, a concentrated winding structure introduces higher MMF harmonics causing additional core losses in the rotor and increases the harmonic distortion of the BEMF. Furthermore, the winding arrangement can be classified into a single-layer winding or a double-layer winding. In a single-layer winding, each stator slot is occupied by one coil side, while in a double-layer winding, each slot contains two vertically or horizontally divided winding sets. Figure 2.5 shows the winding arrangement of a concentrated double-layer winding for a 12 slot, 8 pole PMSM.

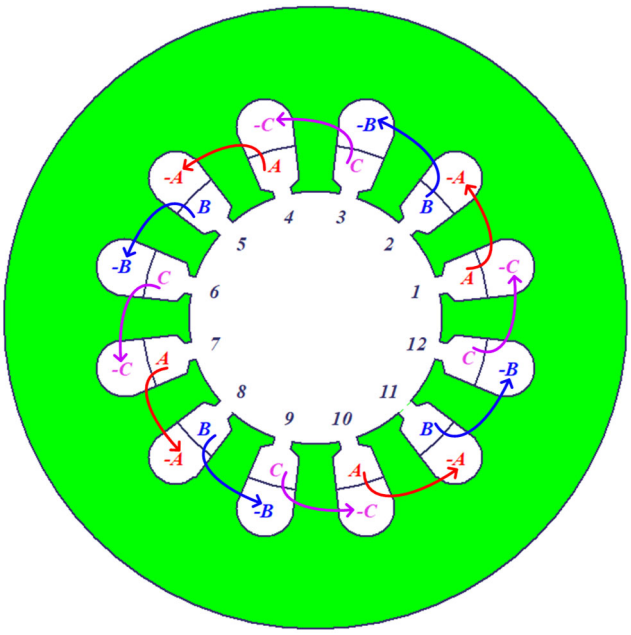

Figure 2.5 Concentrated double-layer winding for a 12 slot 8 pole PMSM

As seen in Figure 2.5, each stator slot has two coil sides from two different phases and the opposite end of each coil is located in the adjacent stator slot. Therefore, the windings of a specific phase are not overlapped with the other phases' windings in this type of concentrated winding pattern.

For further analysis, a detailed model of IPMSM in d-q reference frame can be derived starting from stator's time-domain equations. The equations of stator phase voltages can be expressed as follows using Kirchhoff's Voltage Law (KVL) and Faraday's laws.

$$v_{\mathrm{a}} = R_{\mathrm{s}} i_{\mathrm{a}} + \frac{d}{dt}(\lambda_{\mathrm{a}}) \tag{2.1}$$

$$v_{\mathrm{b}} = R_{\mathrm{s}} i_{\mathrm{b}} + \frac{d}{dt}(\lambda_{\mathrm{b}}) \tag{2.2}$$

$$v_{\mathrm{c}} = R_{\mathrm{s}} i_{\mathrm{c}} + \frac{d}{dt}(\lambda_{\mathrm{c}}) \tag{2.3}$$

The flux linkage of each phase of the winding due to PMs can be expressed through the following equations.

$$\lambda_{pma} = \lambda_{pm}\cos(\theta_r) \tag{2.4}$$

$$\lambda_{pmb} = \lambda_{pm}\cos(\theta_r - 2\pi/3) \tag{2.5}$$

$$\lambda_{pma} = \lambda_{pm}\cos(\theta_r - 4\pi/3) \tag{2.6}$$

The total flux linkage equations of phase A, phase B, and phase C are as follows.

$$\lambda_a = L_{aa}i_a + L_{ab}i_b + L_{ac}i_c + \lambda_{pma} \tag{2.7}$$

$$\lambda_b = L_{ba}i_a + L_{bb}i_b + L_{bc}i_c + \lambda_{pmb} \tag{2.8}$$

$$\lambda_c = L_{ca}i_a + L_{cb}i_b + L_{cc}i_c + \lambda_{pmc} \tag{2.9}$$

The rotor angle (θ_r) is the angle between synchronously rotating q-axis and stationary phase A axis of the stator. The equations for time-domain voltages and flux linkage are converted to d-q reference frame using Park's Transformations as described in (2.10) and (2.11). The X_a, X_b and X_c can be any three-phase time varying quantity (voltage, current, flux linkage) and X_d, X_q and X_0 are the corresponding d-q domain quantities. The d-q coordinate system of the IPMSM is represented in Figure 2.6.

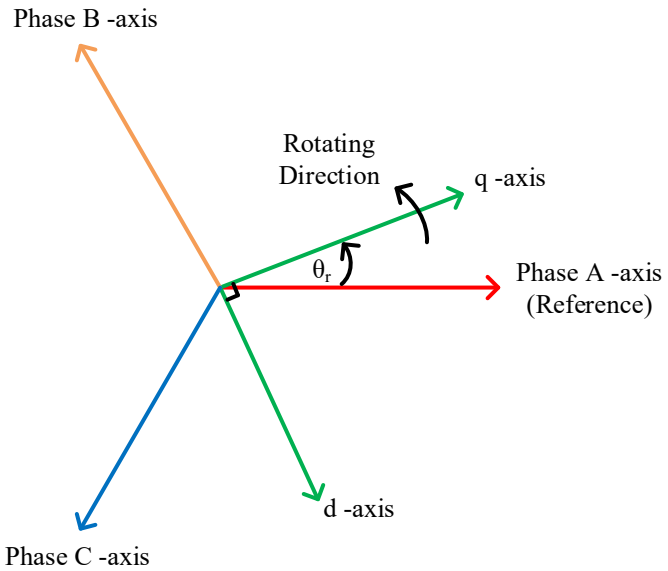

Figure 2.6 Stator three phases and d-q reference frame

$$\begin{bmatrix} X_a \\ X_b \\ X_c \end{bmatrix} = \frac{2}{3}\begin{bmatrix} \cos(\theta_r) & \cos(\theta_r - 2\pi/3) & \cos(\theta_r - 4\pi/3) \\ \sin(\theta_r) & \sin(\theta_r - 2\pi/3) & \sin(\theta_r - 4\pi/3) \\ 1/2 & 1/2 & 1/2 \end{bmatrix}\begin{bmatrix} X_q \\ X_d \\ X_0 \end{bmatrix} \tag{2.10}$$

$$\begin{bmatrix} X_q \\ X_d \\ X_0 \end{bmatrix} = \begin{bmatrix} \cos(\theta_r) & \sin(\theta_r) & 1 \\ \cos(\theta_r - 2\pi/3) & \sin(\theta_r - 2\pi/3) & 1 \\ \cos(\theta_r - 4\pi/3) & \sin(\theta_r - 4\pi/3) & 1 \end{bmatrix}\begin{bmatrix} X_a \\ X_b \\ X_c \end{bmatrix} \tag{2.11}$$

The voltages and flux linkage equations of the IPMSM in d-q reference frame are shown in (2.12), (2.13), (2.14) and (2.15) [25].

$$v_d = R_s i_d - \omega_e \lambda_q + \frac{d\lambda_d}{dt} \tag{2.12}$$

$$v_q = R_s i_q + \omega_e \lambda_d + \frac{d\lambda_q}{dt} \tag{2.13}$$

$$\lambda_d = \lambda_{pm} + L_d i_d \tag{2.14}$$

$$\lambda_d = L_q i_q \tag{2.15}$$

The $\frac{d\lambda_d}{dt}$ and $\frac{d\lambda_q}{dt}$ terms of (2.12) and (2.13) are considered to be zero in steady state operation and accordingly the steady state voltage equations can be written as follows:

$$v_{md} = R_s i_d - \omega_e L_q i_q \tag{2.16}$$

$$v_{mq} = R_s i_q + \omega_e \lambda_{pm} + \omega_e L_d i_d \tag{2.17}$$

The electromagnetic torque can be expressed using d- and q-axis flux linkages and currents as follows [14]:

$$T_e = \frac{3}{2}\frac{p}{2}\left[\lambda_d i_q - \lambda_q i_d\right] \tag{2.18}$$

By substituting (2.14) and (2.15) in (2.18), T_e can be expanded as follows:

$$T_e = \frac{3}{2}\frac{p}{2}\left[\lambda_{pm} i_q + (L_d - L_q) i_d i_q\right] \tag{2.19}$$

Up to this point all electromagnetic equations in d-q reference frame are derived assuming ideal conditions and neglecting the effects of saturation, losses, and harmonics.

2.3 Speed Control of IPMSM in Constant Torque and Field Weakening Regions

The speed control methods of PMSM can be mainly divided into two categories, i.e., scalar control and vector control. Scalar control is accomplished by changing the magnitude and frequency of the stator voltage. Scalar control can be implemented in both open-loop and closed-loop forms while it lacks improving the dynamic response of the system. However, it is a simple and cheap method to implement and it is mainly used in simple applications such as motor drives in pump and fan applications [20]. The most popular scalar control method of PMSM is V/f control method, which is achieved by maintaining the ratio of the voltage and frequency constant up to the rated voltage and frequency [21].

The fundamental principle of the vector control method is to control both the magnitude and phase angle of the stator current simultaneously. The vector control method is a closed-loop control approach, which requires more complex sets of controllers to improve the dynamic response of the system. Therefore, vector control method is more popular in applications that require high performance such as EVs and railway transportation systems [22, 23]. There are two main vector control techniques for PMSM, namely FOC and Direct Torque Control (DTC). The FOC is employed by decoupling the flux and torque of the machine and controlling those two quantities separately [24]. FOC requires to have a position sensor, which gives the rotor position information to the control system. In DTC, flux and torque of the machine are directly controlled by changing

the stator voltage [25]. DTC does not require a position sensor, because there are separate control blocks to extract the rotor position using signal processing methods. The classification of speed control methods is briefly shown in Figure 2.7.

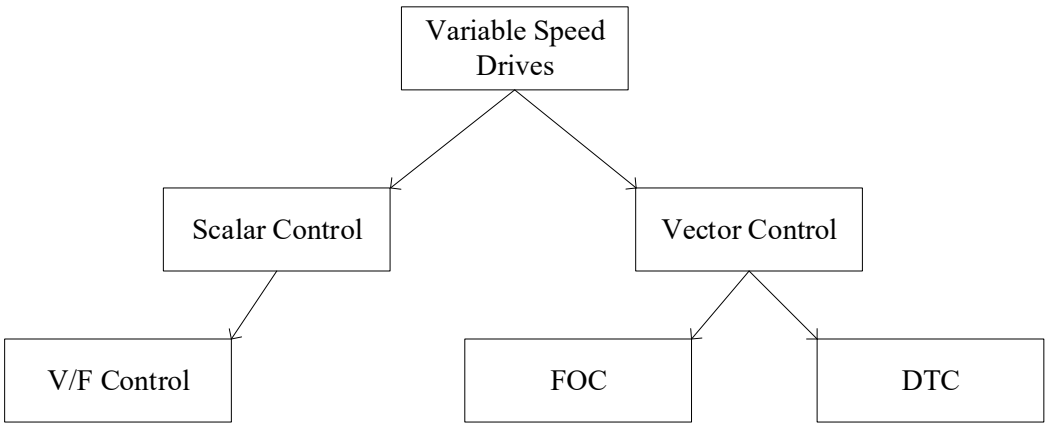

Figure 2.7 Classification of speed control methods

FOC method is one of the most prominent control approaches widely used in IPMSM drives. In different literature, various speed control algorithms are discussed to control the machine in constant torque region and FW region using FOC technique.

According to different performance requirements, the following control strategies can be classified for a PMSM:

- Constant Torque Angle Control [14, 15]
- Unity Power Factor Control [14, 15, 26]
- Constant Air-Gap Mutual Flux-linkages Control [14, 15]
- MTPA Control [14, 27]
- FW Control [14, 28, 29]

The Constant Torque Angle Control is achieved by maintaining the torque angle of the machine at 90 degrees. The 90-degree torque angle can be accomplished by setting d-axis current to be on zero. Accordingly, this method is mainly recommended for control of SPMSMs below the base speed operating region. In Unity Power Factor Control method, the inverter is fully

utilized for providing active power to the PMSM. It can be done by controlling the torque angle of the machine as a function of motor variables. The Constant Mutual Flux Linkage Control is achieved by maintaining the resultant flux components from stator and rotor as a fixed value. Normally, this value is kept equal to rotor flux linkage. This control technique can be used in both constant torque region and FW region.

However, in most industrial applications, MTPA Control and FW Control are extensively used in a wide speed range. Furthermore, FW control algorithms can be classified into three different sub-algorithms. In literature these techniques are identified as follows.

- Constant Voltage Constant Power (CVCP) Control [30]
- Constant Current Constant Power (CCCP) Control [31]
- Optimum Current Vector (OCV) Control or Voltage Current Limited Maximum Torque (VCLMT) Control [32]

The CVCP and CCCP control methods are more popular for SPMSMs, while VCLMT control technique is a useful method for both IPMSMs and SPMSMs. In CVCP control method, both voltage and output power are kept at their constant values by changing the current vector following the constant power current trajectory in d-q reference frame. The CCCP control is achieved by keeping both current and output power as constants by changing the q-axis component of the voltage.

In this thesis, MTPA and VCLMT control techniques are used for control of IPMSM in a wide speed range.

2.3.1 MTPA Control Technique

The aim of MTPA control is to maximize the developed torque of the machine in the constant torque region for a given stator current. For a given stator current, there is a unique d- and q-axis

current pair that maximizes the developed torque of the machine. The maximum developed torque is limited by the maximum allowed phase current. The voltage constraints are not important in this case due to the low-speed operating points. It is important to note that the MTPA control technique improves the motor drive's efficiency by minimizing the machine's copper losses while maximizing its developed torque simultaneously.

The current trajectory of an IPMSM in MTPA region is illustrated in Figure 2.8, while the current angle is denoted by β and the peak current of the stator is denoted by I_{max}. The current circles in Figure 2.8 illustrate the different stator currents. The torque contour that has the maximum value and can intersect with corresponding current circles defines the maximum developed torque at each level of the stator current. These intersection points actually define the path of the MTPA trajectory. The current angle of the machine increases versus developed torque enhancement in the MTPA region.

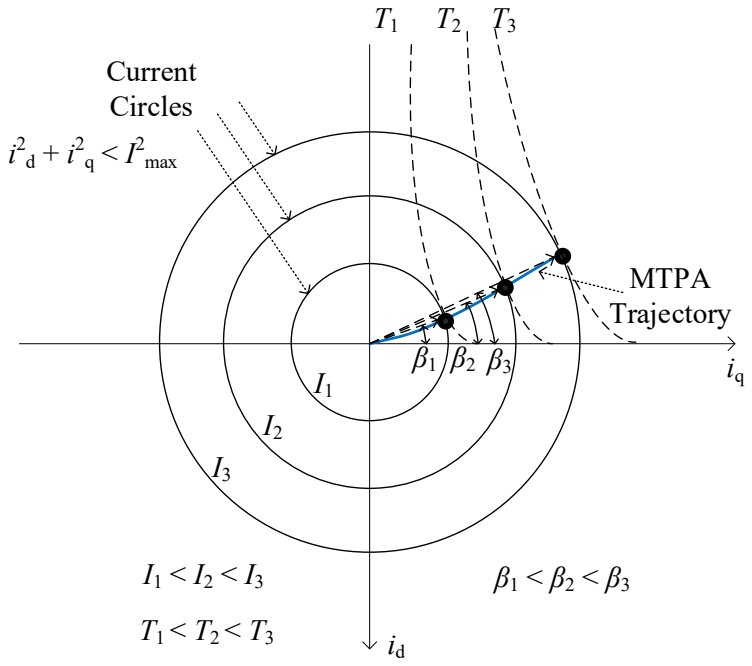

Figure 2.8 Current trajectory, current circles, and torque tracks in MTPA region/control

2.3.2 VCLMT Control Technique

The principal concept of the VCLMT control technique is similar to MTPA control technique. It maximizes the output torque of the machine in FW region with a minimum possible drawn stator current. As in MTPA control, drive efficiency is maximized in VCLMT control. The developed torque in FW region is limited by the maximum available voltage and allowed phase currents.

According to (2.17), $\omega_e\lambda_{pm}$ term (BEMF of the machine) increases with speed and it contributes to an increase in the motor terminal voltage at high speeds. The $\omega_e L_d i_d$ term helps to compensate this increasing BEMF by weakening the field by applying a large negative d-axis current.

The current trajectory of VCLMT control technique is illustrated in Figure 2.9.

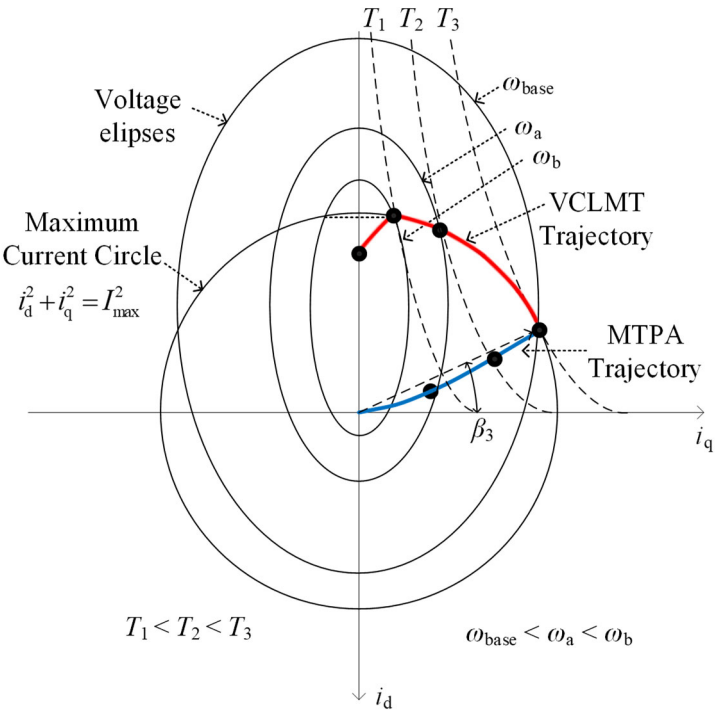

Figure 2.9 Current trajectory, voltage ellipses, and torque tracks for VCLMT control

The voltage of the IPMSM in d-q reference frame can be represented as an ellipse. The voltage ellipses shrink with the increment of the machine's speed. The value of a torque contour

intersecting the voltage ellipses and maximum current circle provides the maximum developed torque of the machine in that specific operating speed.

2.3.3 Challenges and Motivations in MTPA and VCLMT Control

According to (2.16), the developed torque of an IPMSM is a function of d- and q-axis currents. Therefore, it is necessary to ensure the machine operates with an appropriate combination of d- and q-axis currents to provide the expected efficient performance in MTPA and VCLMT control regions. Thus, it is important to obtain an optimized d-axis reference current trajectory in a wide speed range to achieve a desired performance for the machine. It is worth noting that, q-axis current is automatically adjusted based on the defined d-axis reference current and required torque. However, in actual operation of an IPMSM the inductances and PM flux linkage are not fixed under different loading conditions and all of the parameters used in torque and voltage equations may vary with the saturation of the stator core [33, 34]. In addition, core losses [35, 36] and solid losses [37] (due to skin, proximity, and magnet loss effects) show non-linear variations and are dependent on the behaviour of the magnetic field distribution and operating frequency of the machine. Therefore, it is important to consider these electromagnetic losses in predicting accurate characteristics of the machine and d-axis reference current in a wider speed range application. According to this discussion, an optimized d-axis reference current trajectory needs to take into account the saturation and losses effects to support satisfactory performance for IPMSMs in a wide speed range.

In literature various control approaches have been investigated to come up with a satisfactory performance prediction method for IPMSMs in both constant torque and FW regions. Authors in [38, 39] and [40] have introduced an ideal d-axis reference currents (neglecting non-linearities and losses) in both MTPA and FW regions in their analysis. As a result of assuming ideal conditions,

larger discrepancies may appear between the analysis and experimental tests. For instance, the ideal d-axis reference current for MTPA and VCLMT control techniques are shown in (2.20) and (2.21), respectively, [38] while L_d, L_q and λ_{pm} are all assumed to be fixed in (2.20) and (2.21).

$$i_{d,ref} = \frac{-\lambda_{pm} + \sqrt{\lambda_{pm}^2 + 8(L_d - L_q)I_{max}^2}}{4(L_d - L_q)I_{max}^2} \tag{2.20}$$

$$i_{d,ref} = \frac{-\lambda_{pm} L_d + \sqrt{\lambda_{pm}^2 L_d^2 - (L_d^2 - L_q^2)[\lambda_{pm}^2 + L_q^2 I_{max}^2 - (\frac{V_{max}^2}{\omega_e})^2]}}{(L_d^2 - L_q^2)} \tag{2.21}$$

Ching-Tsai Pan and S. M. Sue have proposed a linear MTPA control strategy to obtain fast-dynamic response [41] and it helps to reduce the complexity of the controller. This linear approach is useful when controlling multiple IPMSMs synchronously. Even though the analysis is extended to FW region the effect of the core saturation and high frequency losses, e.g., core losses and solid losses, are not considered in the analysis and performance prediction.

Authors in [42], [43] and [44] have considered the saturation effect of the machine into their analysis using online parameter estimation methods. The controllers used in their analysis are capable of estimating real-time machine parameters such as inductances. The whole analysis is based on assuming a fixed PM flux linkage. References [42] and [43] have addressed the issues of d-axis inductance variations and cross saturation in simulation and experiments. Additionally, [42] considered the effect of the temperature variation in their study. However, these two analyses are only limited to MTPA operation and FW region is not considered during the performance analysis steps. Authors in [44] have extended the analysis to FW region and considered the d- and q-axis flux saturation and temperature sensitivities in the parameter estimation algorithm. However, the analyses in [44] do not report the significance of the different electromagnetic and mechanical losses in FW region. A similar analysis has been done in [45] for both MTPA and FW regions

using adaptive control techniques. In [45], the flux control algorithms are developed for operations in a wide speed range and control algorithms and stability of the system are demonstrated using Lyapunov Stability Criterion and Barbalat's Lemma. The analysis in [45] does not report any details regarding the saturation effects and losses of the machine. Another online torque control method is described in [46] for both MTPA and FW regions using optimization techniques and Ferrari's solution method. The analysis in [46] takes into account the effects of core saturation by considering the variation of inductance. The copper losses and core losses are considered as well in the analysis. However, [46] has ignored the effects of solid loss and mechanical losses in the study which is not a reasonable assumption especially in FW region.

Y. Kim and S. Sul have proposed torque control strategy for a PMSM using PM flux variations [47]. The authors have developed a PM flux estimator using flux observer which uses two current reference lookup tables for different PM flux linkage and generate the new reference currents by using an interpolation method. The analysis is extended to full operating region in the constant torque operating region for different temperature levels. The research presented in [48] describes a method of extending the speed range of a PMSM in MTPA region. The errors that originate from the inverter side are compensated to measure the d- and q-axis flux linkages accurately. The d- and q-axis reference currents are generated using an optimization solution. The effect of the saturation is included in the analysis by incorporating d- and q-axis flux linkages in the analysis. Authors in both [47, 48] have neglected some important losses, i.e. core losses, solid losses, and mechanical losses in the analysis, which may significantly affect the performance prediction of the machine at higher speeds.

In both [49] and [50], authors have estimated the performance of a PMSM considering machine's saturation and cross coupling effects. However, the analysis is only limited to MTPA

region. The authors in [49] and [50] have captured the d-axis and q-axis flux linkage variations using Finite Element Analysis (FEA). The equations are formulated for calculating the d-axis and q-axis currents using flux linkage variations and curve fitting techniques. Thereafter, the trajectory of the MTPA control region has been obtained. Another similar analysis is done by T. Inoue, Y. Inoue, et al. to propose a mathematical model for controlling PMSM in MTPA region [51]. The authors have proposed a mathematical methodology to determine the parameters of the machine model and determine the trajectory of MTPA control by taking into account the magnetic saturation and cross coupling effect. However, the proposed model estimates the PM flux linkage and authors do not address the validity of their control approach and performance prediction in FW region.

In [52] and [53] the maximum efficiency operating points are tracked for a PMSM drive by applying the non-linear optimization techniques. The analyses are done in MTPA operating points of the machine. Authors in [52] have included the variation of the copper loss and core loss into their analysis and the circuit model of the PMSM has been modified accordingly. The d-axis and q-axis currents are calculated based on non-linear optimization methods. In [53], the core saturation effect, cross coupling effect, copper losses, core losses and other inverter losses are considered to predict the trajectory of loss minimal current reference in MTPA region for PMSM drives. However, authors in [52, 53] have focused only on MTPA operating region in their studies.

Another analysis is done in [54], [55], and [56] to improve the efficiency of the PMSM drive system by optimizing the stator current. The authors in [54] have developed iron losses minimization strategy in the controller to minimize the total losses of the system in FW region. They have developed an iron losses model by collecting the data using standardized Epstein measurement data. In addition, copper losses and mechanical losses are included in [54]. However,

authors in [54] have ignored the solid losses, which affect the performance prediction of the machine significantly in FW region. In [55], authors are focused on SPMSM and stator current is controlled to minimize the torque ripple of the machine in MTPA operating region. The method is efficient in computation point of view with simultaneously reducing the losses and torque ripple of the machine in MTPA region. No details are found in [55] regarding the performance of the system in FW region. In addition, both [54, 55] have considered the inductances as fixed values in the whole analysis while neglecting the effect of core saturation. Although the method proposed in [56] can be extended to FW region, the authors optimize the stator current vector for a given reference torque to minimize the copper losses. In addition to that, this technique can be implemented as a real time application. It is worth noting that [56] does not show any details regarding the simulation or experiment results in FW region.

According to the literature review reported in this section, most of the references have only conducted performance prediction and control analysis only either in MTPA or FW region while normally the effects of solid, mechanical, and core losses in FW regions are neglected. In this thesis, not only are the effect of saturation and losses taken into account for accurate performance prediction and d-axis reference current trajectory, but also the analysis is extended to cover both MTPA and FW regions in a wide speed range.

2.4 Conventional Single Inverter Motor Drive and its Control Method

In a conventional single inverter motor drive system, the wye-connected IPMSM is fed by only one VSC capable of providing both required active and reactive powers to the machine in MTPA and FW regions. The example vector diagrams are shown in Figure 2.10 illustrating the voltage and current vectors lie in d-q reference frame for both lagging and leading power factor operations of the machine.

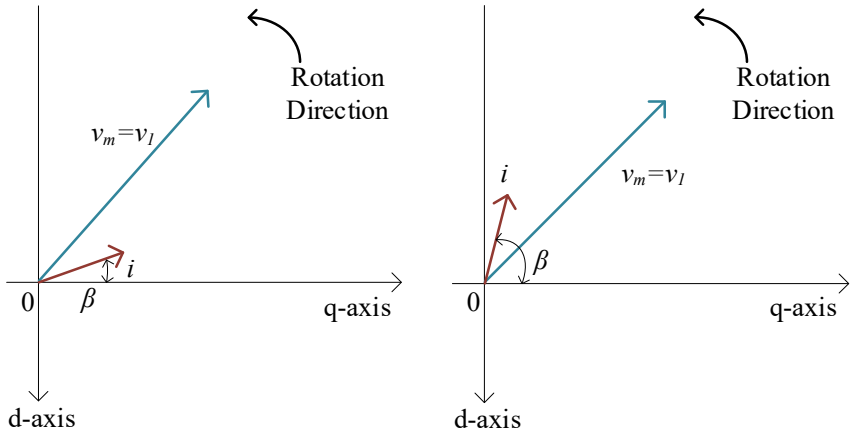

Figure 2.10 Example vector diagrams for a single inverter motor drive system, (a) lagging power factor and (b) leading power factor

The basic control block diagram of a single inverter motor drive is shown in Figure 2.11 for both MTPA and FW regions. The d-axis reference current may be set by a lookup table in each operating speed and developed torque based on an optimized current trajectory extraction. The outer speed loop defines the reference speed, and the output of the PI speed controller defines the q-axis reference current accordingly. Both d- and q-axis current controllers generate the d- and q-axis voltages, which are required to feed the machine using a VSC. The rotor angle is measured by the incremental encoder, and rotor speed is evaluated using the measured rotor angle. The rotor position information is sent to coordinate transformations blocks to convert the voltage/current quantities from abc domain to d-q domain. The d- and q-axis components of the monitored currents are calculated using the measured three phase currents and “a-b-c to d-q” transformation block. The controller’s generated d- and q-axis voltage components are transformed to abc domain using “d-q to a-b-c” transformation block. The time domain voltage signals are used to determine the modulation index and the frequency of the inverter.

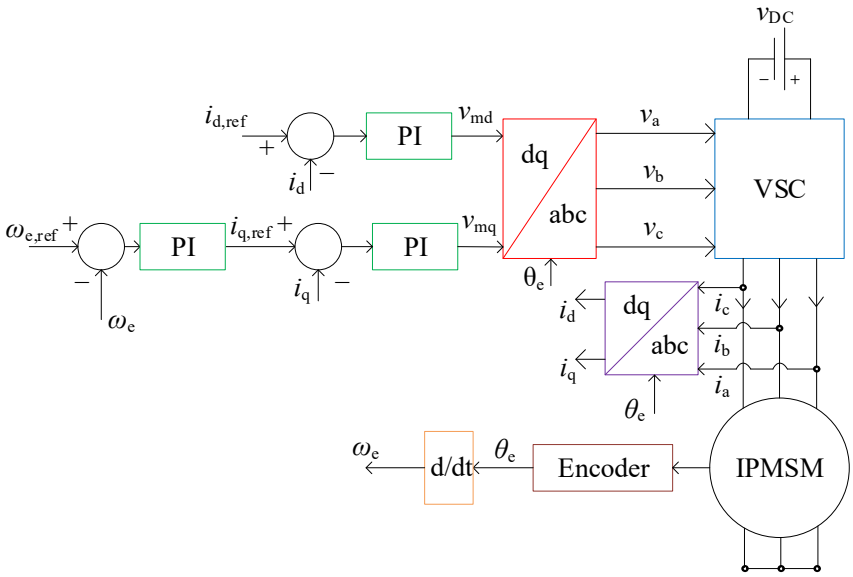

Figure 2.11 Control block diagram of a single inverter motor drive system

2.5 Summary

PMSM was introduced as one of the main sub-categories of PM machines. The presence of the reluctance torque component in the total developed torque was highlighted as the main advantage of the IPMSMs over the SPMSMs. Time domain voltage and current equations of the IPMSM were introduced and then transferred into the rotating d-q reference frame using Park's Transformation. The steady state equation of the ideal developed torque of IPMSM was formulized neglecting the non-linearities and losses effects.

The basic control strategies of PMSMs were investigated and FOC was introduced as one the most popular control techniques for PMSMs in a wide speed range. The MTPA and VCLMT control algorithms were selected for machine's operation in the constant torque and FW regions respectively, while maximizing the developed torque in the minimized copper losses and drawn current taking into account the current and voltage limitations. The ideal d-axis reference current trajectories in both MTPA and VCLMT control approaches were analytically formulized and introduced neglecting the machine's saturation and losses.

Example voltage-current vector diagrams were shown to explain the single inverter motor drive operation in d-q reference frame, and the control block diagram was presented to show how an IPMSM can be controlled in a wide speed range using a VSC.

Chapter 3

Effects of Saturation and Losses on the Predicted Performance of an IPMSM

In this chapter, an IPMSM is simulated using ANSYS-Maxwell V.18.2 and the variations of inductances, PM flux linkage, and different losses are predicted in various loading levels and speed ranges via electromagnetic FEA. The steady state developed torque equation is introduced taking into account all of the investigated saturation and loss effects. The operating capabilities of a conventional single inverter motor drive system is compared with the dual inverter OW motor counterparts. The machine used in the analysis is a V-shaped magnet IPMSM. The main parameters of this machine and its simulated flux density distribution in the rated speed and power operating condition are described in Table 3.1 and Figure 3.1, respectively.

Table 3.1 Main parameters of the IPMSM

Parameter	**Value**	**Parameter**	**Value**
Power	1 kW	Number of slots	12
Voltage (L-L)	220 V	Number of poles	8
Rated current	3.5 A	Conductor	AWG 18
Rated speed	900 rpm	Lamination	M19-29G
Power factor	0.9	Magnet	NdFeB35

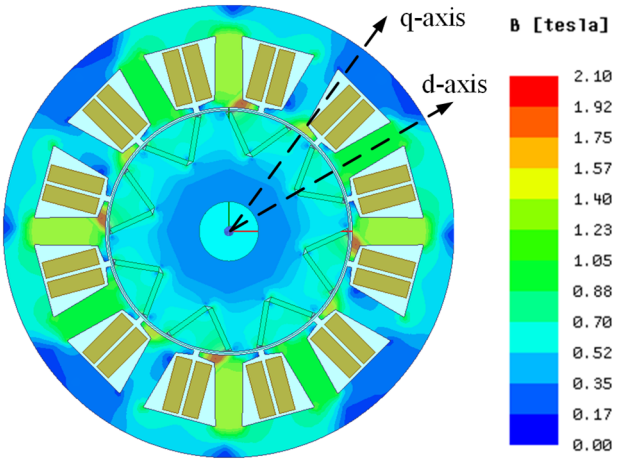

Figure 3.1 Flux distribution of the analysed IPMSM at the rated operating point

3.1 Effects of Saturation on the Inductances and PM Flux Linkage

The core's saturation directly depends on the excitation or loading level of the IPMSM, which even causes the PM flux linkage to vary during the machine's performance in various operating points. In addition, loading and saturation effects cause the inductance of the machine to significantly vary and affect the saliency ratio as well. The reluctance torque component of an IPMSM is directly a function of the saliency ratio. Moreover, the PM flux linkage is the most important factor for the magnetic torque component of the machine. Hence neglecting the inductance variation and PM flux linkage variation can introduce a significant disagreement between the experimental and ideal predicted performance capabilities of the machine

The d- and q-axis inductances (L_d and L_q) and PM flux linkage of the analysed IPMSM are extracted using a Finite Element model developed in ANSYS-Maxwell. The simulations are conducted by exciting the stator windings of the machine with three-phase currents in which the current peak may vary between 0 A to 5 A and the current angle varies from 0° to 90^0. The d- and q-axis inductances, PM Flux linkage and saliency ratio (L_q/L_d) are extracted at each loading point of the machine corresponding to the applied current settings. The variation of d- and q-axis inductances, PM Flux linkage and saliency ratio are shown in Figure 3.2.

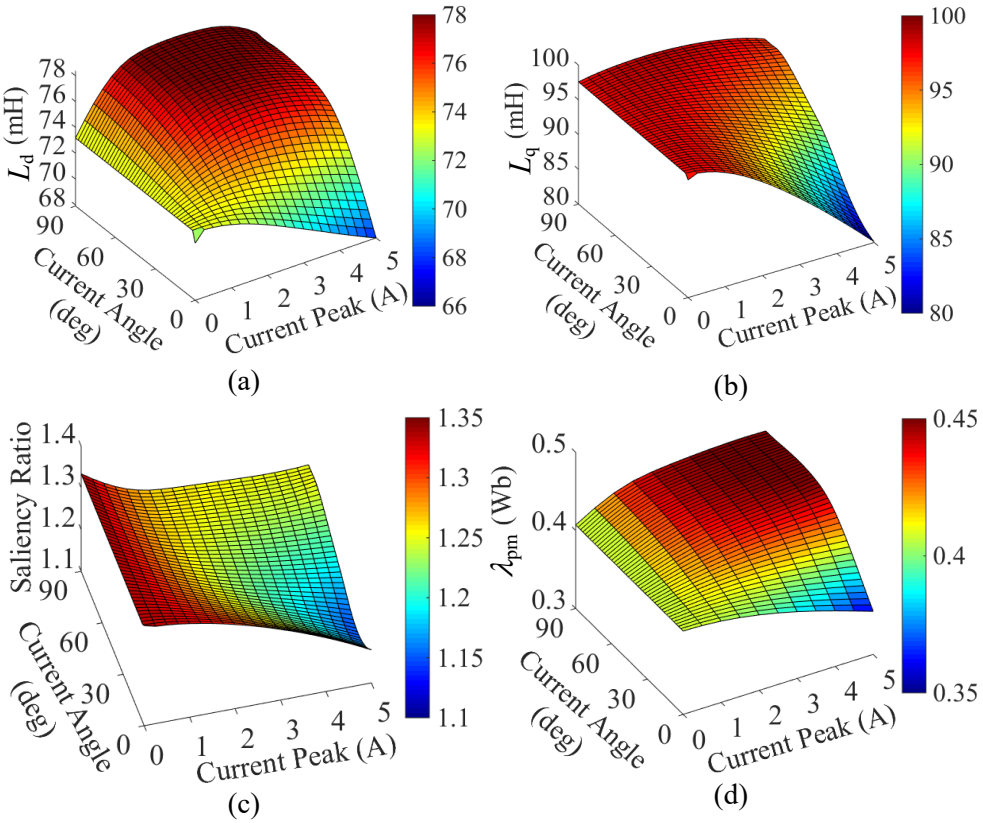

Figure 3.2 Variations of (a) d-axis inductance, (b) q-axis inductance, (c) saliency ratio (L_q/L_d) and (d) PM flux linkage versus current angle and peak changes

A noticeable variation in L_d, L_q, and saliency ratio is seen as a function of current peak and angle changes. For example, by changing the current peaks at lower angles (0-30 degrees) L_d reduces from 73 mH to 66 mH, and L_q reduces from 100 mH to 80 mH. Accordingly, the saliency ratio also decreases from 1.35 to 1.1 in this area. At larger current angles (30-90 degrees), L_d increases from 72 mH to 78 mH, while an extensive change in L_q is not seen in this area. Accordingly, the saliency ratio reduces from 1.35 to 1.22 as the L_q does not effectively change, while L_d is reduced in this area. At higher current angles (30-90 degrees) d-axis current increases causing the field to be weakened; that is why a larger L_d is seen. At lower current angles (0-30 degrees) the q-axis component is actually the main component of the current, and by increasing the current peak in this area the q-axis path becomes more magnetized and therefore L_q reduces significantly.

Although, there is no direct method to measure or calculate the PM flux linkage in loaded conditions, the d-axis flux linkage and inductance can be used to indirectly assess it. According to Figure 3.2(d), the variation of PM flux linkage is somehow similar to the L_d variation. At high current angles and current peaks, a larger amount of PM flux linkage (0.45 Wb) is expected as the d-axis flux path becomes more demagnetized. In the saturated d-axis flux path occurring in lower current angles and higher current peaks, the PM flux linkage reduces from 0.4 Wb to as low as 0.35 Wb. It is important to note that effect of the temperature on PM flux linkage variation is omitted in this analysis, because the copper loss of the simulated and fabricated machine is minimized. The fabricated machine has an open structure, which facilitates air flow and ventilation to help lower any temperature rise due to small losses.

According to the analysis of this section, it is clearly seen that the saliency ratio and PM flux linkage of the machine change by up to 22% and 28%, respectively, depending on the machine's loading condition and magnetic saturation.

3.2 Variation of Losses

DC copper losses of a machine are only a function of DC resistance and the current peak. Therefore, their prediction does not need an extensive magnetic analysis. On the other hand, core and solid losses of the machine are functions of frequency and flux distribution in the cores and windings. To accurately analyse these losses, Finite Element simulations are necessary. In this section, it is shown how the core and solid losses are affected in various loading conditions and frequencies.

The core loss can be separated into two main components: i) Hysteresis loss, ii) Eddy current loss. The common equations for core loss including hysteresis and eddy current losses are show in (3.1), (3.2) and (3.3) [57].

$$P_{hys} = af_e B_p^x \tag{3.1}$$

$$P_{eddy} = bf_e^2 B_p^2 \tag{3.2}$$

$$P_{core} = P_{hys} + P_{eddy} \tag{3.3}$$

Constants a, b, and x in (3.1) and (3.2) are called Steinmetz coefficients, which depend on the type of the material and frequency.

Figure 3.3 shows the core losses variations of the machine at 200 rpm, 900 rpm (base speed), 2000 rpm, and 3300 rpm for various current peaks and current angles. According to Figure 3.3, it is seen that the core losses of the machine change from 0 W to 2 W, 2 W to 10 W, 5 W to 25 W, and 10 W to 50 W for speeds of 200 rpm, 900 rpm, 2000 rpm, and 3300 rpm, respectively.

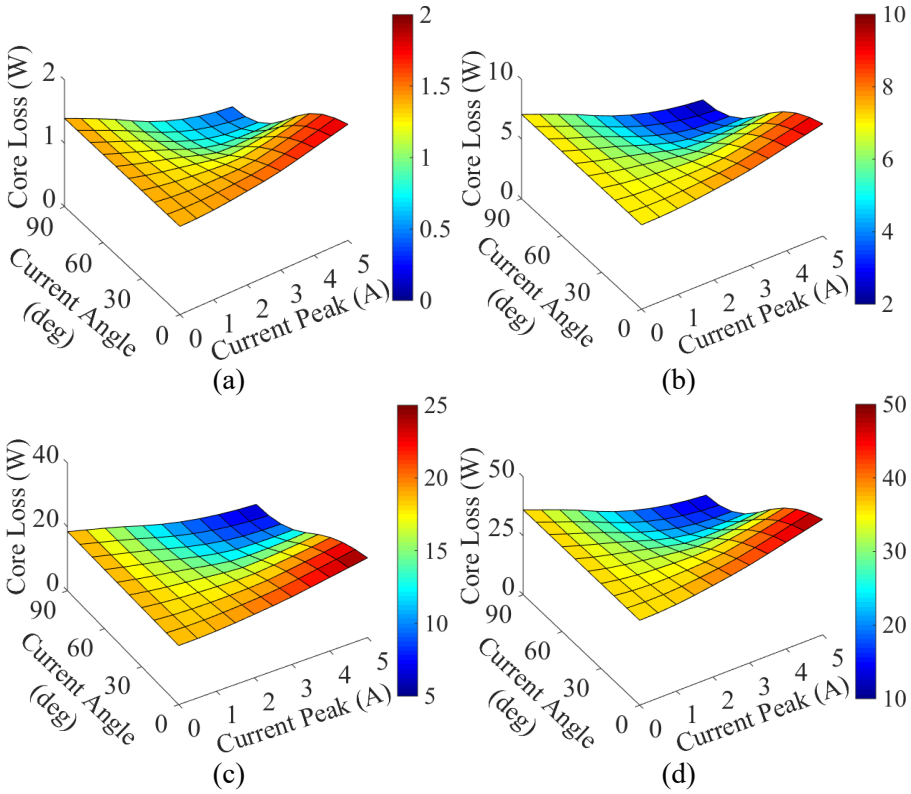

Figure 3.3 Core loss variation versus current peak and current angle changes in (a) 200 rpm, (b) 900 rpm, (c) 2000 rpm, and (d) 3300 rpm

It is shown that by the speed increment the core losses increase. At lower current angles (0-30 degrees), core losses increase along with the current peak increment as in this case the core of

the machine becomes more magnetized. At higher current angles (30-90 degrees), core losses are reduced by increment in the current peak, as a larger d-axis (or field weakening) current is applied.

Figure 3.4 shows the solid losses variations at 200 rpm, 900 rpm (base speed), 2000 rpm, and 3300 rpm for various current peaks and current angles.

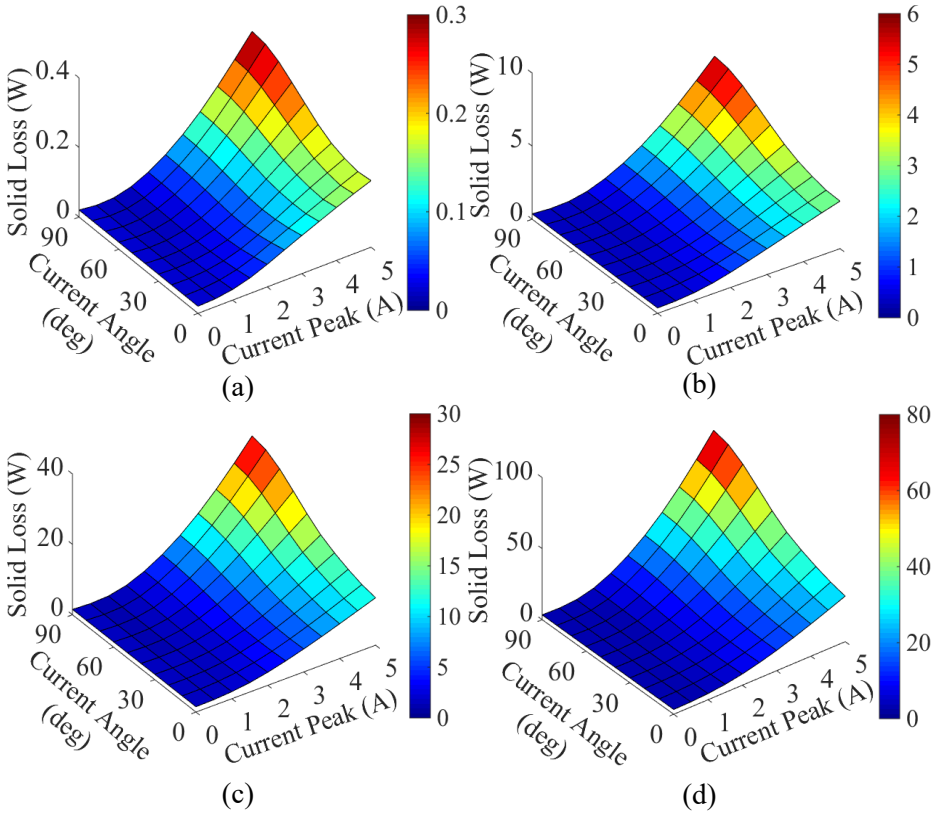

Figure 3.4 Solid loss variation versus current peak and current angle changes in, (a) 200 rpm, (b) 900 rpm, (c) 2000 rpm, and (d) 3300 rpm

According to Figure 3.4, solid losses nonlinearly change versus current peak and angle changes, and by increasing the frequency their effects are more significant. For example, solid losses change from 0 W to 0.3 W, 0 W to 6 W, 0 W to 30 W, and 0 W to 80 W at the speeds of 200 rpm, 900 rpm, 2000 rpm, and 3300 rpm, respectively. It is obvious that the solid losses in low currents and speeds are negligible, while by increasing the speed and current peak these losses are by no means negligible. By increasing the current peak, the AC resistive losses (due to skin effect)

are increased, and by increasing the current angle stator and rotor fluxes oppose each other resulting in a larger flux leakage and more significant proximity losses.

It is worth noting that the core and solid losses profiles were only shown for four speeds due to space limitations. However, these calculations have been done for 65 operating speeds, 11 current peak steps and 10 current angle steps of the machine. Therefore, 7150 total simulations were run to obtain the losses and are incorporated into the analysis.

According to the analysis of this section, it is clearly seen that core and solid losses of the machine may change by up to 5% and 8% of the rated power, respectively, depending on the machine's loading condition, magnetic saturation, and frequency.

3.3 Integrating the Effects of Saturation and Losses in Machine's Performance Prediction

In this section, all of the discussed nonlinearities and losses are taken into account to fulfil MTPA and VCLMT control techniques for the whole speed range of the machine. Inductances, PM flux linkage, core, solid, copper, and mechanical losses as functions of current peak, current angle, and speed are shown as follows.

$$L_{\mathrm{d}} = L_{\mathrm{d}}(i_{\mathrm{peak}}, \beta) \tag{3.4}$$

$$L_{\mathrm{q}} = L_{\mathrm{q}}(i_{\mathrm{peak}}, \beta) \tag{3.5}$$

$$\lambda_{\mathrm{pm}} = \lambda_{\mathrm{pm}}(i_{\mathrm{peak}}, \beta) \tag{3.6}$$

$$P_{\mathrm{core}} = P_{\mathrm{core}}(i_{\mathrm{peak}}, \beta, \omega_{\mathrm{m}}) \tag{3.7}$$

$$P_{\mathrm{solid}} = P_{\mathrm{solid}}(i_{\mathrm{peak}}, \beta, \omega_{\mathrm{m}}) \tag{3.8}$$

$$P_{\mathrm{cu}} = \frac{3}{2} R_{\mathrm{s}} i_{\mathrm{peak}}^2 = \frac{3}{2} R_{\mathrm{s}} (i_{\mathrm{d}}^2 + i_{\mathrm{q}}^2) \tag{3.9}$$

$$P_{\mathrm{mech}} = P_{\mathrm{mech}}(\omega_{\mathrm{m}}) \tag{3.10}$$

P_{mech} variation in (3.10) is defined based on a third order approximation as a function of machine's speed considering a 10 W measured mechanical losses in the rated speed. The effect of core saturation (the inductance variation) can be included into the steady state d- and q-axis voltage equations as follows.

$$v_{md} = R_s i_d - \omega_e L_q(i_{peak}, \beta) i_q \tag{3.11}$$

$$v_{mq} = R_s i_d + \omega_e \lambda_{pm}(i_{peak}, \beta) + \omega_e L_d(i_{peak}, \beta) i_d \tag{3.12}$$

The active and reactive power input of the IPMSM in d-q reference frame are expressed in (3.13) and (3.14).

$$P_m = \frac{3}{2}(v_{md} i_d + v_{mq} i_q) \tag{3.13}$$

$$Q_m = \frac{3}{2}(v_{mq} i_d - v_{md} i_q) \tag{3.14}$$

The active output power of the IPMSM including all considered losses can be expressed as follows.

$$P_{out} = P_m - P_{cu} - P_{core} - P_{solid} - P_{mech} \tag{3.15}$$

The developed torque equation of the IPMSM can be expressed as follows, which includes all discussed non-linearities and losses.

$$T_{dev} = \frac{P_{out}}{\omega_m} \tag{3.16}$$

$$\begin{aligned} T_{dev} = {} & \frac{3}{2}\frac{p}{2}\left\{\lambda_{pm}(i_{peak}, \beta) i_q + \left[L_d(i_{peak}, \beta) - L_q(i_{peak}, \beta) i_d i_q\right]\right\} \\ & - \frac{1}{\omega_m}\left[P_{core} + P_{solid} + P_{mech}\right] \end{aligned} \tag{3.17}$$

The main objective of MTPA control is to maximize the developed torque of the machine under the speeds below base speed (900 rpm) by minimizing the stator phase currents. In MTPA

control, IPMSM is operated at low speeds, as a result of that voltage constraints are not necessary to be considered in all MTPA operating points. The developed torque is limited by maximum allowed stator current limit. The voltages and currents of IPMSM in d-q reference frame are calculated by solving (3.11), (3.12) and (3.17) to obtain the maximum possible torque for a minimum stator current in a given speed. In order to accurately predict the performance capabilities of the machine in MTPA region, a constrained non-linear optimization problem has to be solved which requires a non-linear programming technique taking into account all constraints and Objective Functions (OFs). The formulated non-linear optimization problem for MTPA control algorithm can be expressed by (3.18)-(3.22). The OF is described in (3.18) and all constraints are defined in (3.19)-(3.22).

$$\min\ OF = i_{\mathrm{d}}^2 + i_{\mathrm{q}}^2 \tag{3.18}$$

$$i_{\mathrm{d}}^2 + i_{\mathrm{q}}^2 \le I_{\max}^2 \tag{3.19}$$

$$v_{\mathrm{md}} - R_{\mathrm{s}} i_{\mathrm{d}} - \omega_{\mathrm{e}} L_{\mathrm{q}}(i_{\mathrm{peak}}, \beta) i_{\mathrm{q}} = 0 \tag{3.20}$$

$$v_{\mathrm{mq}} - R_{\mathrm{s}} i_{\mathrm{d}} + \omega_{\mathrm{e}} \lambda_{\mathrm{pm}}(i_{\mathrm{peak}}, \beta) + \omega_{\mathrm{e}} L_{\mathrm{d}}(i_{\mathrm{peak}}, \beta) i_{\mathrm{d}} = 0 \tag{3.21}$$

$$\begin{aligned} T_{\mathrm{dev}} - \frac{3}{2}\frac{p}{2}\left\{\lambda_{\mathrm{pm}}(i_{\mathrm{peak}}, \beta) i_{\mathrm{q}} + \left[L_{\mathrm{d}}(i_{\mathrm{peak}}, \beta) - L_{\mathrm{q}}(i_{\mathrm{peak}}, \beta) i_{\mathrm{d}} i_{\mathrm{q}}\right]\right\} \\ + \frac{1}{\omega_{\mathrm{m}}}\left[P_{\mathrm{core}} + P_{\mathrm{solid}} + P_{\mathrm{mech}}\right] = 0 \end{aligned} \tag{3.22}$$

In FW region, the increasing BEMF of the IPMSM causes the motor voltage to go beyond the maximum allowed terminal voltage determined by the inverter's DC link voltage. However, by applying a larger negative d-axis current it is possible to prevent the increment of the machine's terminal voltage through weakening the air gap flux. Therefore, the voltage constraint becomes one of the main concerning aspects which has to be carefully taken into account in FW region. Accordingly, the maximum possible developed torque in a minimized drawn current is actually

limited by the voltage constraints as well. The VCLMT control algorithm is used to fulfil all described requirements. The same optimization problem as in MTPA control algorithm can be solved to obtain the feasible operating points in FW region with the additional voltage constraint described in (3.23) to take care the terminal voltage of the machine.

$$v_{md}^2 + v_{mq}^2 \leq V_{max}^2 \tag{3.23}$$

It is worth to note that all d- and q-axis inductances, PM flux linkage, core losses, and solid losses computed by FEA are called during the solving steps of the optimization problem. The interior point algorithm, which is an inbuilt function in MTALAB, is used to solve the optimization problems in both constant torque and constant power regions.

3.4 Predicted Performance of IPMSM in MTPA and FW Regions

According to the described algorithms in Section 3.2, the maximum developed torque, output power capability, and d-axis reference current of the machine are derived for both ideal and non-ideal cases in this section. The simulations in this section show the necessity of inclusion of the saturation and losses for performance prediction of IPMSM. In the non-ideal case scenario, all of the variations of PM flux linkage, L_d, L_q, and all considered losses are incorporated in the analysis to predict the capability of the drive system.

The maximum developed torque capability and maximum output power curves for an ideal single inverter drive (i.e., excluding saturation and losses) and a non-ideal case (i.e., including saturation and losses) are shown in Figure 3.5(a) and Figure 3.5(b). In the ideal case, the losses are ignored, and the PM flux linkage, L_d and L_q, are all kept constant using the rated operating point's characteristics.

According to Figure 3.5(a), the developed torque of the ideal case is 0.5 N.m (or 4.4%) larger than the non-ideal case in the constant torque region as all losses and inductance variations are

neglected. In FW region, e.g., at 3000 rpm, the developed torque of the ideal case is 0.8 Nm (or 29%) larger than the non-ideal case. It is seen from the analysis that neglecting the saturation and losses has a significant effect on the performance prediction of an IPMSM especially in high speed operating regions in which the high frequency and mechanical losses are dominant.

According to Figure 3.5(b), in MTPA regions the output powers are close to each other for ideal and non-ideal cases. However, even around 45 W output power difference may be seen between the ideal and non-ideal cases in MTPA region. In FW region, the difference between output powers is more significant and at least 29% difference between ideal and non-ideal output powers is seen at 3000 rpm.

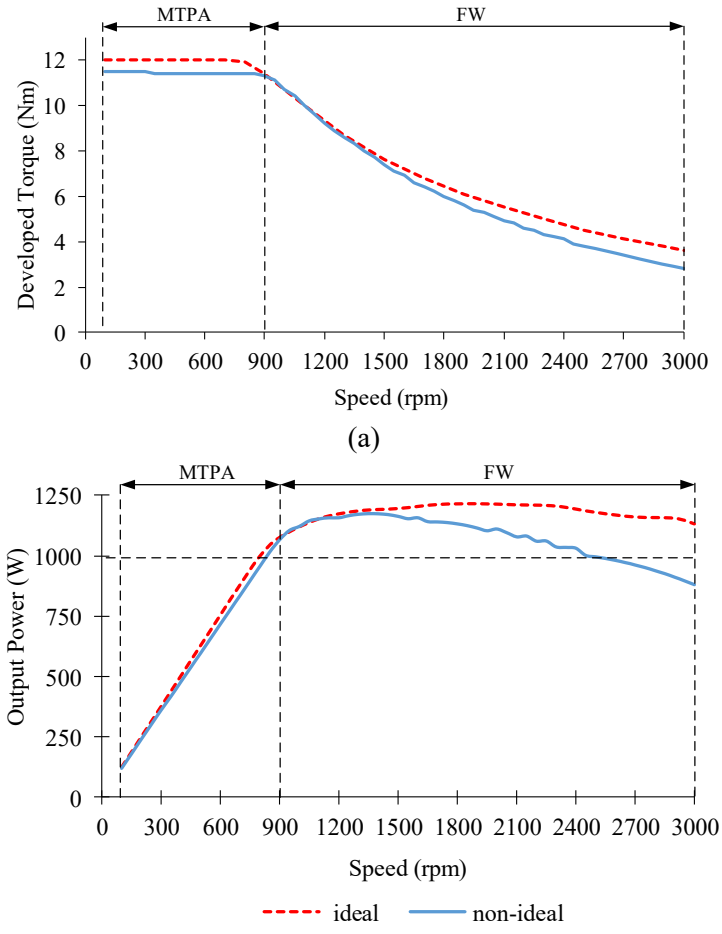

Figure 3.5 (a) Maximum developed torque and (b) Maximum output power for ideal and non-ideal single inverter drive

The d-axis current trajectory in wide range of speeds with (non-ideal) and without (ideal) losses and core nonlinearities are shown in Figure 3.6.

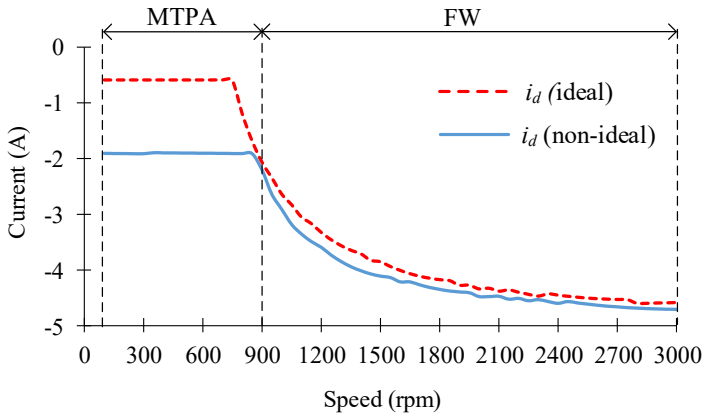

Figure 3.6 d-axis reference current trajectory in the maximum power capability

A noticeable difference (1.3 A) between the ideal and non-ideal d-axis currents is predicted in MTPA region, while this difference is reduced (0.1 A to 0.4 A) at high speeds. It is worth noting that as the terminal voltage of the machine is directly dependent to the d-axis reference current, even a small deviation in the desired d-axis reference current may cause over-modulation problems. The simulations in this section demonstrate the significance of considering losses and inductance and flux changes during performance prediction of an IPMSM.

As a side note, machine's terminal voltage is highly sensitive to d-axis reference current. It is necessary to adjust the d-axis current reference accurately in FW region to prevent the saturation issues in Voltage Source Converter PWM switching mechanism. Because slight deviation of d-axis current can cause the modulation scheme goes from linear to over-modulation region.

3.5 Summary

The effects of saturation on the inductances and PM flux linkage values of the IPMSM in various excitation levels were investigated using FEA. It was shown how the core, solid, and mechanical losses may significantly vary as a function of speed and excitation level of a machine.

The developed torque, output power, and d-axis reference current of the simulated IPMSM were analysed with and without considering saturation and losses effects, and it was shown that neglecting the nonlinearities and losses may have a significant effect on the predicted performance capability of the machine in a wide speed range. The main contribution of this chapter was to show why the nonlinearities and losses should be taken into account during the performance prediction of an IPMSM in MTPA and FW regions.

Chapter 4

Dual Inverter Open Winding Drives

The basic arrangement of a Dual inverter OW IPMSM is introduced in this section and different example circuit topologies of dual inverter motor drives are explained as well. Three OW drives are discussed based on distinguished active/reactive power sharing assumptions and the corresponding control block diagrams are presented for each OW drive structure separately. The predicted performance and capability of the IPMSM for the investigated drive structures are presented for all operating points in MTPA and FW regions.

4.1 Open Winding IPMSM

In conventional AC motor drives, machine's phases are connected in either Star (Wye) or Delta (Δ) arrangement. However, in OW structures, each phase of the windings is opened from both ends and the three open phases are fed by two VSCs. DC links of two inverters can be supported by either battery or a floating capacitor. In this thesis, the first VSC (VSC-1) is considered as the primary energy source and is always supported by a fixed DC voltage. The second VSC (VSC-2) may be fed by another DC voltage source (a battery) or may be connected to a floating capacitor. The basic arrangements of OW IPMSM is shown in Figure 4.1(a), while the effective per phase circuit diagram is illustrated in Figure 4.1(b).

KVL governs the following equations based on Figure 4.1(b).

$$\vec{v}_1 = \vec{v}_m + \vec{v}_2 \tag{4.1}$$

$$v_{1d} - v_{md} - v_{2d} = 0 \tag{4.2}$$

$$v_{1q} - v_{mq} - v_{2q} = 0 \tag{4.3}$$

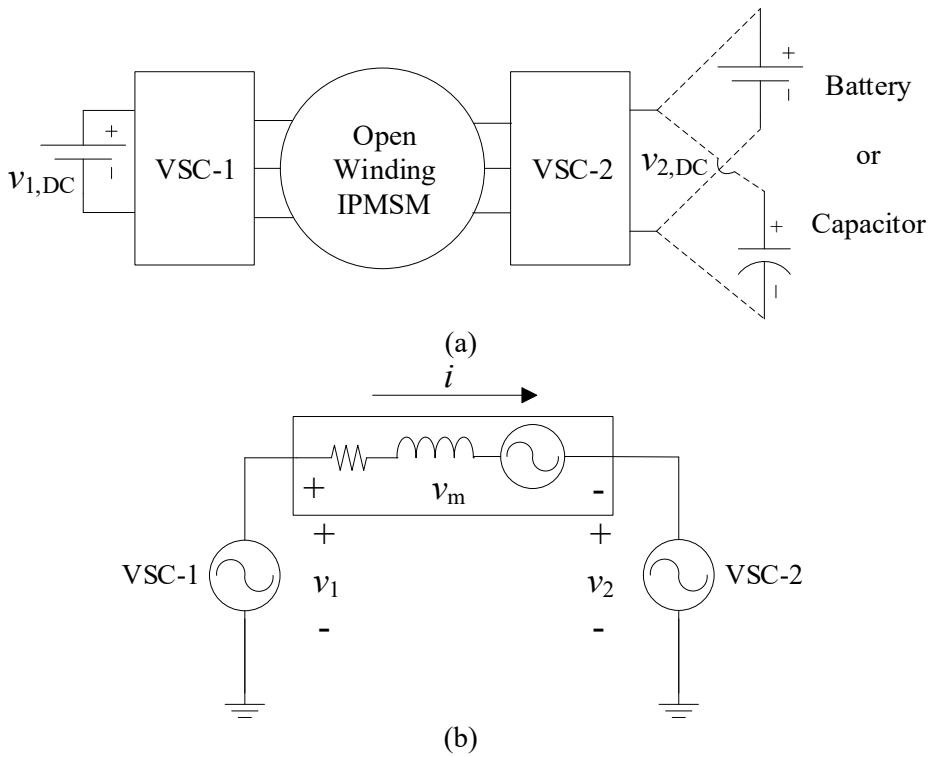

Figure 4.1 (a) Basic arrangement of a dual inverter IPMSM drive and (b) Per phase equivalent circuit

The open winding drive system can be used in different applications such as (i) for machine's operating region extension by supporting the reactive power demands [5], [58-60], (ii) for storing the excess energy in auxiliary energy storage systems in EVs [61-63], (iii) to improve the power quality of MMC based motor drive systems [64], and (iv) to improve the efficiency of distributed energy generation systems [65], which allows to reduce the ratings of the power converters used in the generator system.

According to the connection of the two DC sources of two VSCs, OW drives can be classified into two main categories: (i) Non-isolated Dual Inverter Drive (NDID) and (ii) Isolated Dual Inverter Drive (IDID). The primary advantage of NDID topology is that it requires only a single DC source, however due to having a common DC voltage source, there is a path to flow the zero-sequence currents inside the circuit [66]. As a result of that, there is always a Common Mode Voltage (CMV) component in dual inverter drive circuit [67, 68, 69]. Because of this phenomenon,

noticeable third order harmonics are present in the motor's phase currents. In IDID, there is no path to flow zero sequence currents and negligible third order harmonics are present in the phase currents [61]. However, this topology requires an additional DC source and may need two isolation transformers to make two isolated DC supplies in the power system applications [66]. Figure 4.2 represents the circuit topology of both IDID and NDID.

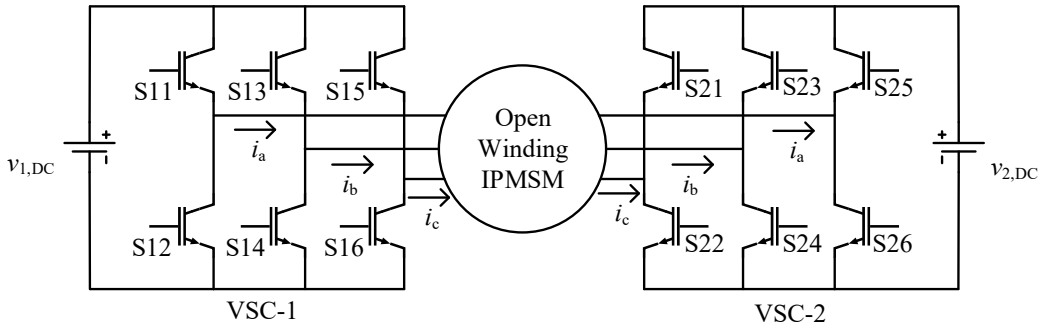

(a)

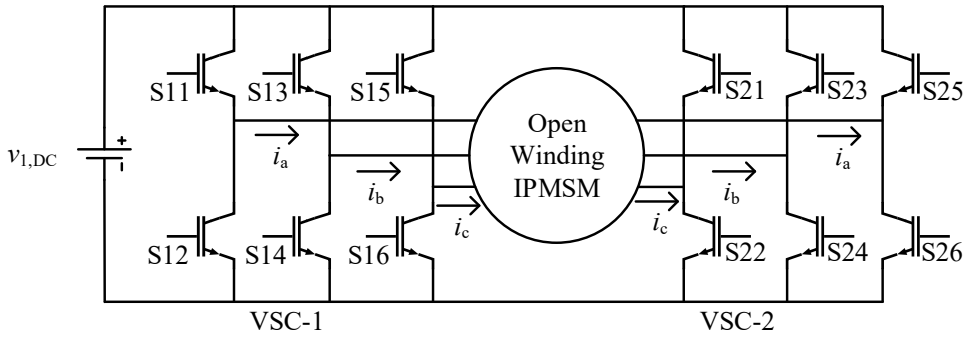

(b)

Figure 4.2 Circuit topologies of, (a) IDID and (b) NIDID

4.2 Challenges and Motivations in Open Winding Motor Drives

In a conventional single inverter drive, there is only one VSC to be controlled and the control strategy is simpler than a dual inverter OW motor drive with two independently controlled VSCs. In recent decades, induction machines are widely used in OW drive structures with different inverter topologies, modulation schemes, and performance improvements attempts [70-73]. Additionally, different control aspects and approaches are already proposed for dual inverter OW

inductions motors [74-75]. However, OW drives have gained lower attention for the PMSM cases. It is important to know how the performance capability and d-axis reference current trajectory of OW IPMSM drives vary in different drive topologies in MTPA and FW regions. In addition, it is also recommended to analyse the performance capability comparison of OW IPMSM drives with a limited available DC link voltage over conventional single inverter drives.

In the existing literature, authors have introduced various methodologies to control the voltage of the inverters in dual inverter OW PMSM drives for speed control applications. Welchko [62] has made a contribution while introducing a dual inverter OW PMSM and proposed three different control methodologies, i.e., unity power factor control method, voltage quadrature control method, and optimum inverter utilization control method, which are based on different active and reactive power sharing assumptions between two inverters. The author has used two isolated inverters with two fixed DC sources. The simulations for the performance analysis for each corresponding control method is presented. However, the analysis has considered fixed inductance values, while neglecting the effect of the core saturation as well as electromagnetic and mechanical losses.

Authors in [5], [58], [59], [76], [77], and [78] have investigated the extension of operating region of a PMSM drive using a dual inverter OW drive as well as providing the voltage control strategies for VSCs. In the drive topologies used in [5], [58], [59], [76] and [77], the DC links of VSC-1 and VSC-2 are supported by a DC source (battery) and a floating capacitor, respectively. The operating capability of the machine (both torque capability and speed range) is extended by increasing the terminal voltage of the machine. The main purpose of having a floating capacitor at the second inverter is to compensate the reactive power requirement of the machine and increase the voltage vector of phase windings without increasing the voltage of the DC source. In [5], a

novel control algorithm has been proposed to control the OW PMSM including voltage controlling of the VSC-2 which contains a floating capacitor. Performance of the controllers in [5] has been verified using both simulations and experiments. The control concepts in [62] is similar to the methods proposed in [5]. In addition to the operating region extension purposes, [58] has used an inverter with a floating capacitor to increase the equivalent inductance of the system to drive the PMSM with a lower operating current compared to its rated operating current. A similar study is done in [58, 59], except the controller is developed using rational functions and VSC-2 is activated at the maximum possible speed of the single inverter drive. The authors in [77] also used an OW PMSM in both MTPA and FW regions. The controller is built using the same concept which has been proposed in [59, 60] to provide the active power from VSC-1 and reactive power from VSC-2. However, according to [5], [58], [76] and [77], it is necessary to use an additional controller to keep the floating capacitor voltage at the desired value.

Other studies have been conducted to extend the power capability and to control the speed of OW PMSM drives with different objectives. For instance, J. S. Park and K. Nam have proposed a dual inverter OW PMSM with a floating capacitor for Hybrid EV (HEV) application [79]. The objective of [79] is to increase the high-speed operating region of the machine by keeping the same battery voltage. The converter that has the floating capacitor compensates the higher reactive power demand of the machine in higher speeds while first inverter operates at a unity power factor. Authors in [80] have proposed a dual inverter OW IPMSM for improving the performance of IPMSM in the constant torque and FW regions. The voltage of the floating capacitor is controlled according to the required performance in FW region. In [78], OW SPMSM is used with two isolated DC link voltage sources. The capability of the machine is enhanced using two separate

DC sources. The investigated controllers have been proposed to operate the machine in FW region and voltage of VSC-2 is controlled using a voltage quadrature control method.

On the other hand, authors in [81] have proposed a hysteresis current regulator to control high power OW PMSM for wind energy generation system using dual half-controlled converters. However, authors do not provide details and explanation about the defined controller. Z. Zheng, D. Sun and J. Zhu have introduced torque ripple minimization control technique for OW PMSM to supress the torque ripples of the machine [82]. The analysis has taken the magnetic saturation effect into account to build a more accurate mathematical model based on harmonic current injection. In [83], authors have proposed model predictive torque control method for OW PMSM. This method has included the non-linearities and constraints into the analysis to minimize the errors. It can implement in real time by reducing the computation time and capable of providing better dynamic response.

Overall, the analyses in [5, 58, 59, 76, 77, 78, 79, 80] have been limited for one OW PMSM drive topology, which has a DC source in VSC-1 and a floating capacitor in VSC-2. However, authors in [78, 81, 83] have analysed OW drive topology, which includes additional DC source instead of using a floating capacitor in second converter. The authors in [82] only addressed a method of including the effect of saturation in OW PMSM drives.

Although the above studies are mainly focused on controlling the voltages of inverters for speed control applications of OW PMSMs, the presented research studies do not contribute to the performance capability analysis comparison for different OW drive topologies with a limited DC link voltage condition in both MTPA and FW regions. In addition, the effects of machine's saturation, magnetic losses, and mechanical losses have never been considered in both MTPA and FW regions in the dual inverter OW IPMSM drives so far. Neglecting these important factors in

the analysis may cause a potential discrepancy between the expected and actual performance of dual inverter OW IPMSM drives. In this thesis, the mentioned shortcomings are resolved to assess the performance capability and operating limits of dual inverter OW PMSM drives in both MTPA and FW regions.

4.3 Dual inverter Drives Cases

In this section, the performance analysis of conventional single inverter and a number of dual inverter OW IPMSM drives are studied considering saturation and loss effects.

4.3.1 Case 1

A common DC voltage source is used in this drive structure and the available DC voltages for both VSCs are set to be half of that in the conventional single inverter drive thus requiring new constraints shown in (4.4) and (4.5). In Both MTPA and FW regions, the required active power is identically shared between the two VSCs as described in (4.6), and VSC-1 may only provide active power governed by (4.7). VSC-1 does not contribute to reactive power support and the required reactive power is solely supported by VSC-2. Performance capability characteristics of the machine in this drive structure in MTPA and FW regions can be derived by solving a similar optimization problem to the single inverter drive case taking into account (4.1)-(4.3) and the new constraints in (4.4)-(4.7).

$$v_{1d}^2 + v_{1q}^2 \le \frac{1}{4} V_{max,single}^2 \tag{4.4}$$

$$v_{2d}^2 + v_{2q}^2 \le \frac{1}{4} V_{max,single}^2 \tag{4.5}$$

$$(v_{1q} + v_{2q}) i_q + (v_{1d} + v_{2d}) i_d = 0 \tag{4.6}$$

$$v_{1q} i_d - v_{1d} i_q = 0 \tag{4.7}$$

Figure 4.3(a) and Figure 4.3(b) illustrate two sample phasor diagrams for *case 1* which describes the arrangement of voltage and current vectors in d-q reference frame in lagging and leading power factor operating points, respectively.

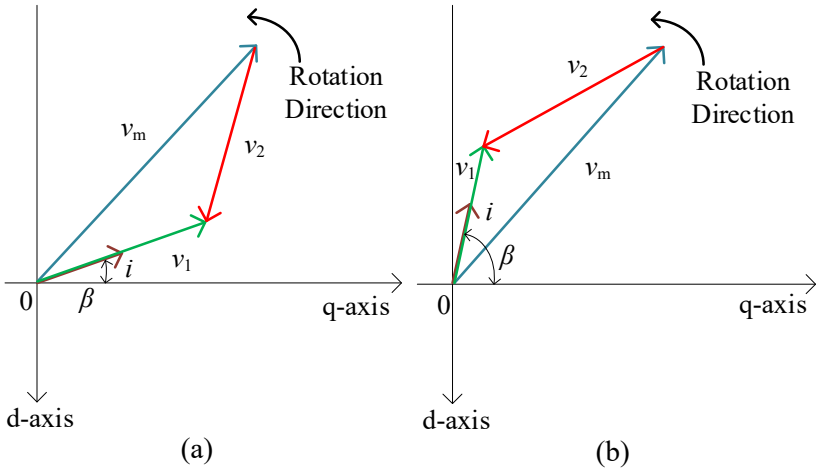

Figure 4.3 Example vector diagrams for *case 1*, (a) Lagging (b) Leading power factor

4.3.2 Case-2

The structure and voltage ratings (i.e., (4.4) and (4.5)) of *case 2* are exactly similar to *case 1*; however, both the required active and reactive power of the machine are identically shared between the two VSCs in MTPA and FW regions. Accordingly, the d- and q-axis voltage components of VSC-1 and VSC-2 are defined as follows.

$$v_{1d} = -v_{2d} = \frac{v_{md}}{2} \tag{4.8}$$

$$v_{1q} = -v_{2q} = \frac{v_{mq}}{2} \tag{4.9}$$

Figure 4.4(a) and Figure 4.4(b) illustrate two sample phasor diagrams for *case 2*, which describes the arrangement of voltage and current vectors in d-q reference frame in lagging and leading power factor operating points, respectively.

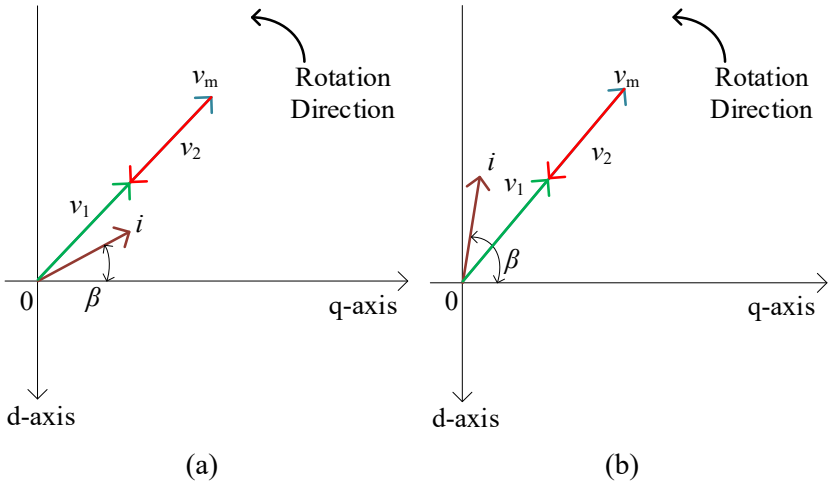

Figure 4.4 Example vector diagram for *case 2*, (a) Lagging and (b) Leading power factor

4.3.3 Case-3

In this drive structure, the DC link of VSC-2 is connected to a floating capacitor. Therefore, the entire required active power of the machine must be supported by VSC-1, while VSC-2 only provides the reactive power of the machine in MTPA and FW regions. The capacitor voltage of VSC-2 and DC link voltage of VSC-1 are both set to half of the DC link voltage of the conventional single inverter drive; hence (4.4)-(4.5) remain valid. Equations (4.7) and (4.10) govern the active power and reactive power requirements, respectively. The capacitor voltage control method has already been investigated in [5], and [19].

$$v_{1d} i_d + v_{2q} i_q = 0 \tag{4.10}$$

In order to show how the voltages are shared in *case 3*, Figure 4.5(a) and Figure 4.5(b) illustrate two sample phasor diagrams in the d-q reference frame for lagging and leading power factor operating points, respectively.

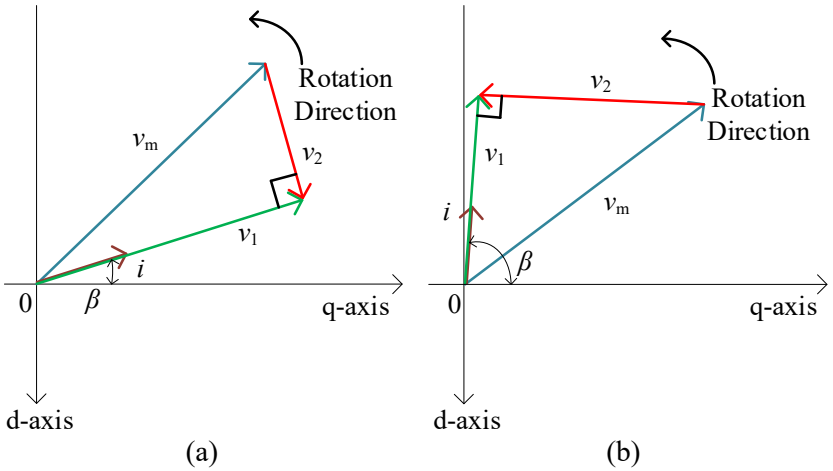

Figure 4.5 Example vector diagram for *case 3*, (a) Lagging and (b) Leading power factor

4.4 Control Diagrams of Dual Inverter Drives

In this section, closed-loop control diagrams for each drive structure are developed for implementation on an experimental test rig to verify the actual performance of machine in each drive for both MTPA and FW regions.

4.4.1 Case-1

The total active (P_m) power of machine is described in d-q reference frame as follows.

$$P_m = \frac{3}{2}(v_d i_d + v_q i_q) \tag{4.11}$$

Since half of the active power of the machine is supported by VSC-1 with no reactive power from this VSC, the d- and q-axis voltage components of VSC-1 are as follows.

$$v_{1d} = \frac{P_m i_d}{3I_m^2} \tag{4.12}$$

$$v_{1q} = \frac{P_m i_q}{3I_m^2} \tag{4.13}$$

where,

$$I_{\mathrm{m}} = \sqrt{i_{\mathrm{d}}^2 + i_{\mathrm{q}}^2} \tag{4.14}$$

Using (4.2), (4.3), (4.12) and (4.13), the d-and q-axis voltage components of VSC-2 are defined. The control block diagram of *case 1* is shown in Figure 4.6. The I_{m}, i_{d} and i_{q} are required to send as inputs of "Voltage Decomposition" block. Additionally, a low-pass filter is required to reduce the ripple of the d-q voltages of VSC-1 and VSC-2 by filtering d- and q-axis currents of the machine.

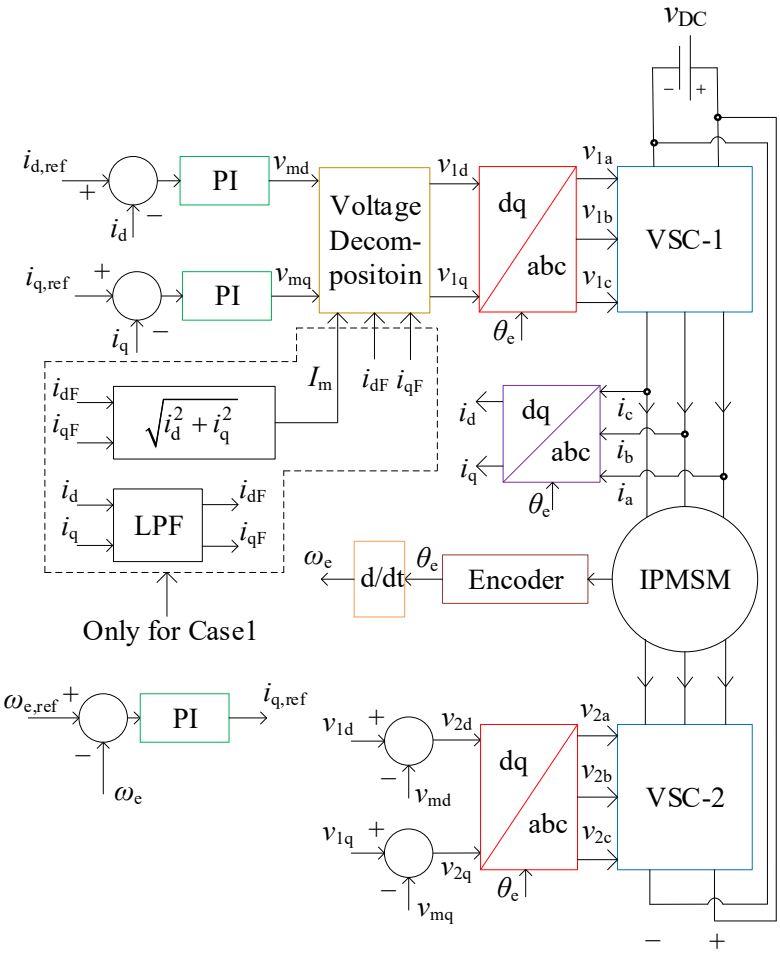

Figure 4.6 Control block diagram of *case 1* and *case 2*

4.4.2 Case-2

In this drive structure, active and reactive power requirements are identically shared between the two VSCs. Accordingly (4.8) and (4.9) are used to define the d- and q-axis voltage components of VSC-1 and VSC-2.

The control block diagram of this drive structure is similar to *case 1* (Figure 4.6). However, the d- and q-axis voltage components of VSC-1 and voltage decomposition block should be modified according to (4.8) add (4.9) and low-pass filter is not required in this case.

4.4.3 Case-3

In this drive structure, one component of the active power is responsible for capacitor voltage charging; therefore, the total active power provided by VSC-1 (P_1) is defined as follows.

$$P_1 = P_m + P_2 \tag{4.15}$$

where P_2 is the output of the capacitor voltage controller. Accordingly, d- and q-axis voltage components of VSC-1 are defined as follows.

$$v_{1\mathrm{d}} = \frac{2P_1 i_{\mathrm{d}}}{3I_{\mathrm{m}}^2} \tag{4.16}$$

$$v_{1\mathrm{q}} = \frac{2P_1 i_{\mathrm{q}}}{3I_{\mathrm{m}}^2} \tag{4.17}$$

Using (4.16), (4.17), (4.2), (4.3), the d- and q-axis voltage components of VSC-2 are defined. The control diagram of Case 3 is shown in Figure 4.7.

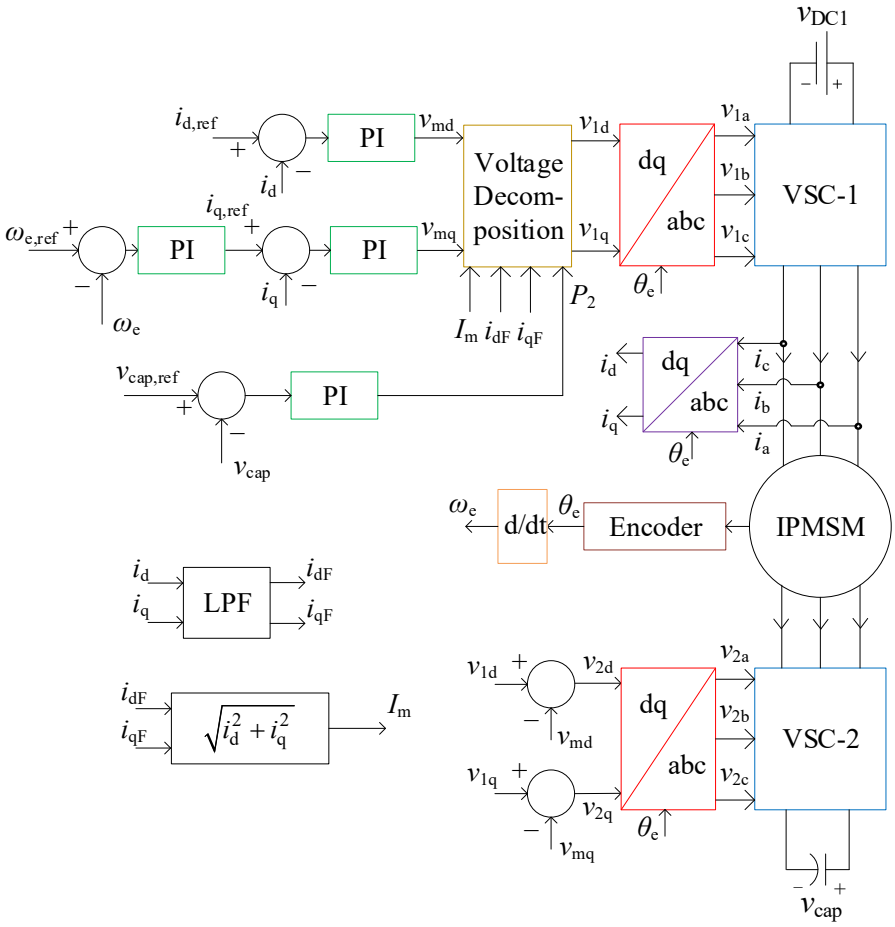

Figure 4.7 Control block diagram of *case 3*

It is worth noting that in all block diagrams defined in this section, the d-axis reference current ($i_{d,ref}$) is set as a look up table by solving optimization problems described in section 4.3 in various speed and developed torque requirements considering dynamic variations of inductance and flux linkages and losses discussed in Chapter 3. It is important to note that the low-pass filter in Figure 4.7 is necessary to reduce the ripple of the d-q voltages of VSC-1 and VSC-2 by filtering d- and q-axis currents of the machine. All controllers are tuned experimentally with the aim of bringing the machine to steady state operation without adverse transient effects.

4.5 Performance Prediction and Comparison of Drive Structures

In this section, the performance of the IPMSM with each drive configuration (including conventional single inverter drive) described in Sections 2.4, 4.3 and 4.4 are predicted at steady state. It is worth noting that the dynamic behaviour of inductances and flux linkages and electromagnetic and mechanical losses are all taken into account, while an average model of VSCs is used in simulations and the harmonic contents of current and 3D effects are neglected for simplicity and a fast simulation.

Figure 4.8 shows d-axis current contour maps versus speed and torque in all operating points of MTPA and FW regions.

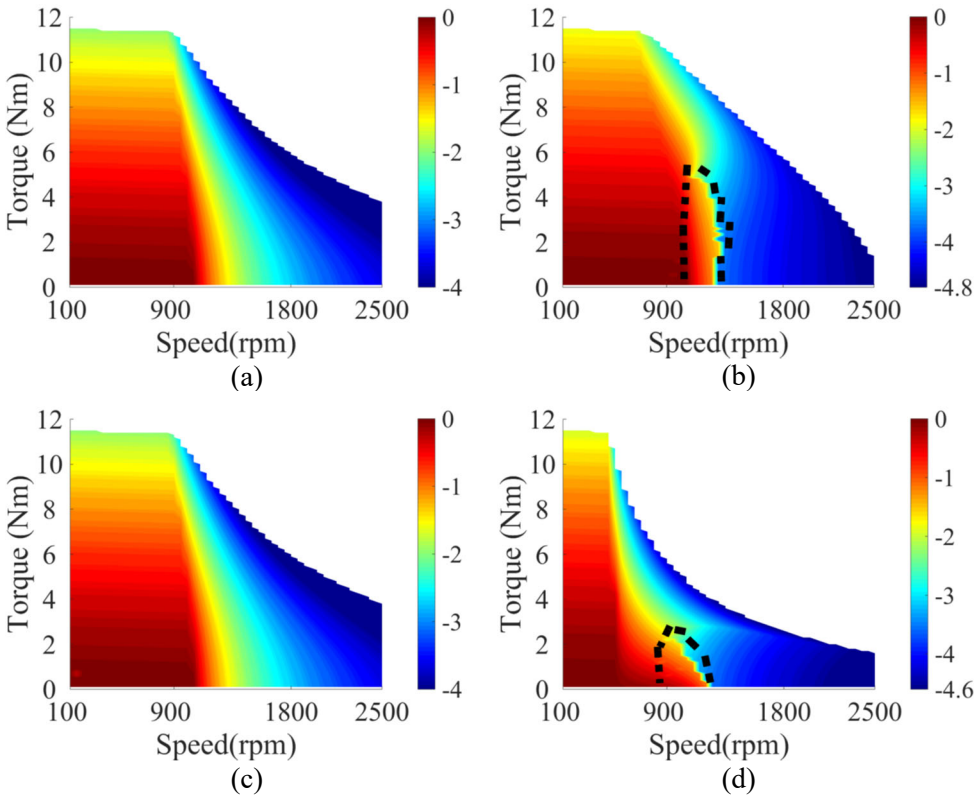

Figure 4.8 d-axis current contour maps versus speed and torque variations, (a) single inverter, (b) *case 1*, (c) *case 2* and (d) *case 3*

According to Figure 4.8, all drive configurations are capable to support 11.4 Nm developed torque in the constant torque or MTPA region; however, single inverter and *case 2* are the two

drives that support this torque up to 900 rpm. The maximum speed at which 11.4 Nm developed torque can be supported by *case 1* and *case 3* are 700 rpm and 450 rpm, respectively. Due to the equal available voltages in single inverter and *case 2* drives in all operating points, these two drive configurations show identical torque capabilities and speed ranges. On the other hand, the available voltages on machine's phases in *case 1* and *case 3* are smaller than that of the single inverter drive due to the smaller DC voltages and assumed active and reactive power sharing requirements. In all drive configurations, d-axis reference current may change from 0 A to even -4 A to -4.8 A depending on the operating region and developed torque. In MTPA regions d-axis current is limited to around -2 A, while in FW regions this current should be even doubled to keep the machine's terminal voltage within the converter's rating.

The efficiency of the machine can be evaluated as follows.

$$Eff\,(\%) = \frac{P_{\text{out}}}{P_{\text{out}} + P_{\text{cu}} + P_{\text{core}} + P_{\text{solid}} + P_{\text{mech}}} \times 100 \tag{4.18}$$

The variation of efficiency for all cases are illustrated in Figure 4.9. According to Figure 4.9, Single inverter, *case 1* and *case 2* drives can operate with same peak efficiency of 93.5%. The peak efficiency region of three drives are concentrated between 3-8 Nm torque and 500-1200 rpm speed. However, *case 3* drive operates with 92.6 % peak efficiency. Both Single inverter and *case 2* have same efficiency variation, because those two drive cases show same identical voltage and performance capabilities throughout their entire regions. In MTPA region, the efficiency is lower than 80% at the peak torque for the speeds below 300 rpm. Because the develop output power is relatively small for low speed operating points. In FW region, efficiency starts to drop below 85% beyond 2000 rpm of all drives due to dominant core, solid and mechanical losses.

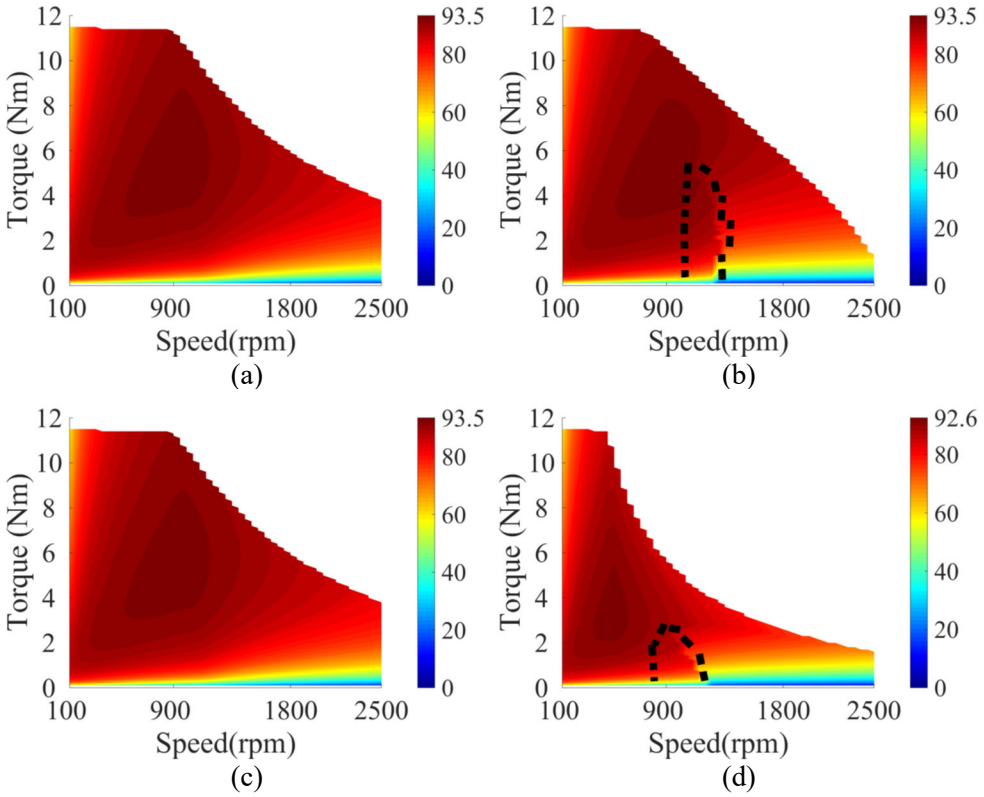

Figure 4.9 Efficiency contour maps versus speed and torque variations, (a) single inverter, (b) *case 1*, (c) *case 2* and (d) *case 3*

The power factor variations for different drive structures are shown in Figure 4.10. The power factor may change from 0.12 to unity depending on the operating point. According to the active and reactive power sharing assumptions for each drive configuration, the control strategies of *case 1* and *case 3* drive structures should be slightly modified as the required reactive power of the machine cannot be solely supported by VSC-2. In these operating points, which are distinguished inside a black dashed line in all contour maps, the VSC-1's unity power factor assumption is no longer valid, and a part of the machine's reactive power has to be supported by VSC-1 as well. The control strategies and active and reactive power sharing assumptions of single inverter and *case 1* need no modification in any operating point. According to Figure 4.10, the highest possible power factor (> 0.97) is seen in MTPA regions with the developed torques below 3 Nm for all

drives and in FW regions up to 1800 rpm and 900 rpm for single inverter, *Cases 1* and 2, and *case 3* drives, respectively.

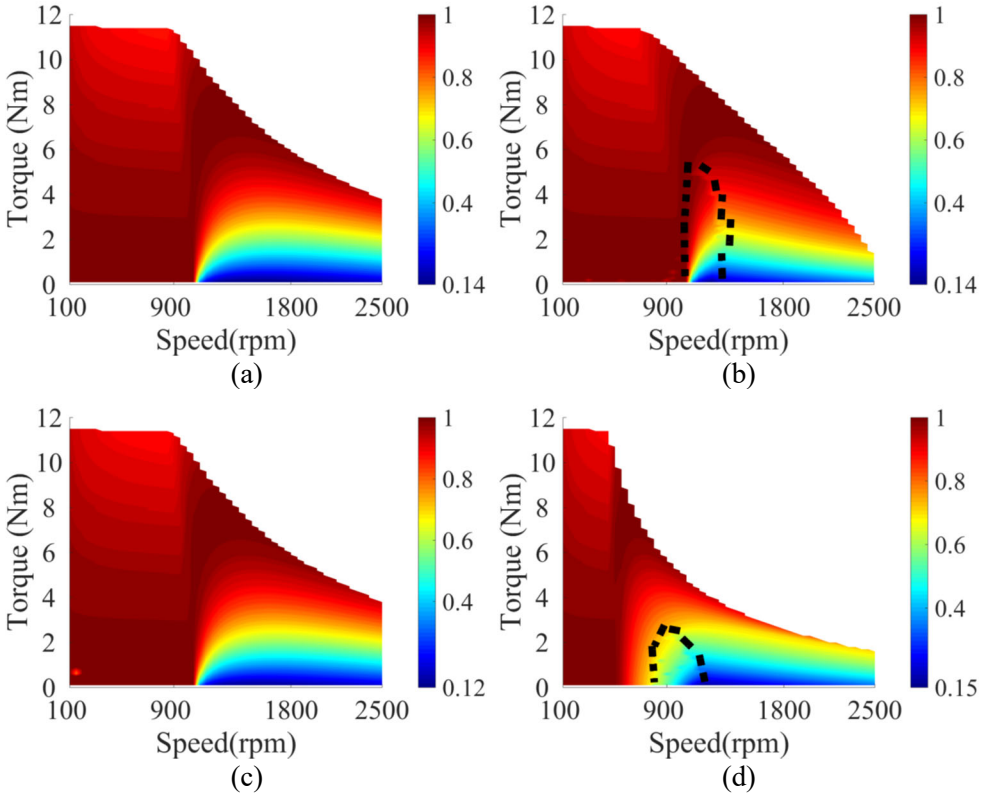

Figure 4.10 Power factor contour maps versus speed and torque variations, (a) single inverter, (b) *case 1*, (c) *case 2* and (d) *case 3*

The reactive power sharing of all drive cases is illustrated in Figure 4.11. In MTPA regions the supported reactive power by VSCs enhance along with the torque increment even up to 602 Var, 452 Var, 301 Var, and 315 Var for the VSC used in single inverter drive, VSC-2 in *case 1*, each of VSC-1 and VSC-2 in *case 2*, and VSC-2 in *case 3*, respectively. In FW region, VSCs gradually start to absorb reactive power even up to 950 Var, 630 Var, 475 Var, and 640 Var for the VSC used in single inverter drive, VSC-2 in *case 1*, each of VSC-1 and VSC-2 in *case 2*, and VSC-2 in *case 3*, respectively, because of the leading power factor performance of the machine.

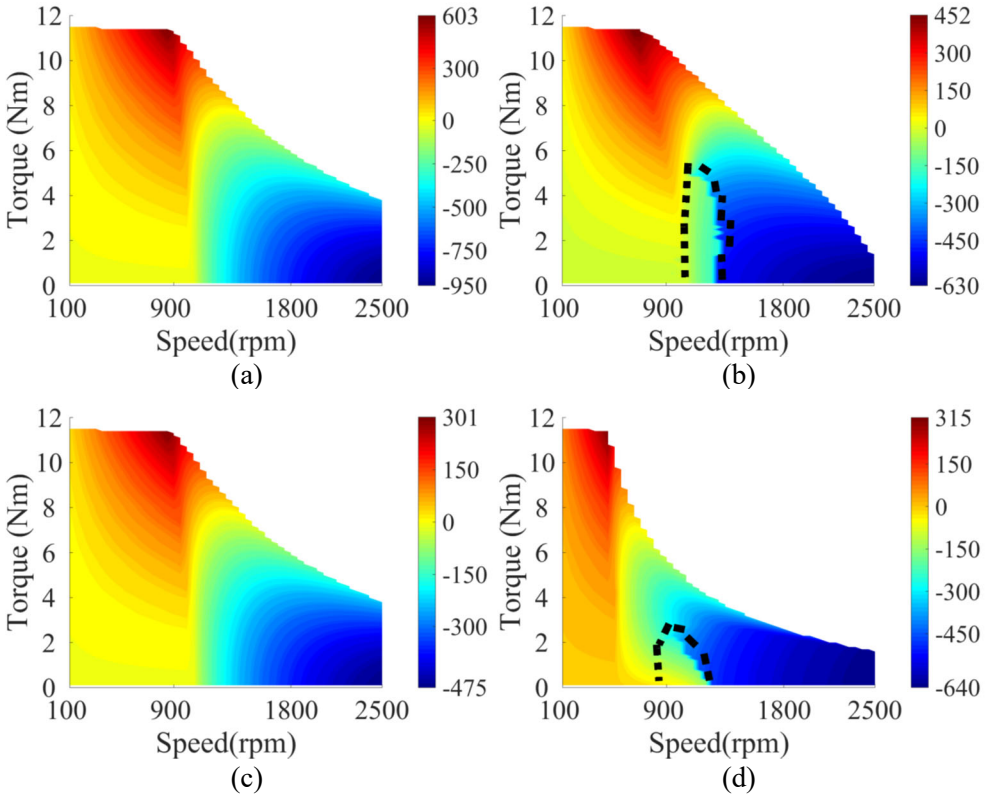

Figure 4.11 Reactive power contour maps versus speed and torque variations, (a) single inverter, (b) *case 1*, (c) *case 2* and (d) *case 3*

The active power sharing of all drive cases is illustrated in Figure 4.12. The peak power of the machine in single inverter drive may reach 1265 W, while up to 633 W output power can be separately provided by VSC-1 and VSC-2 in Cases 1 and 2. The only source of active power in *case 3* is VSC-1, and the maximum developed power of machine in this case is limited to 649 W.

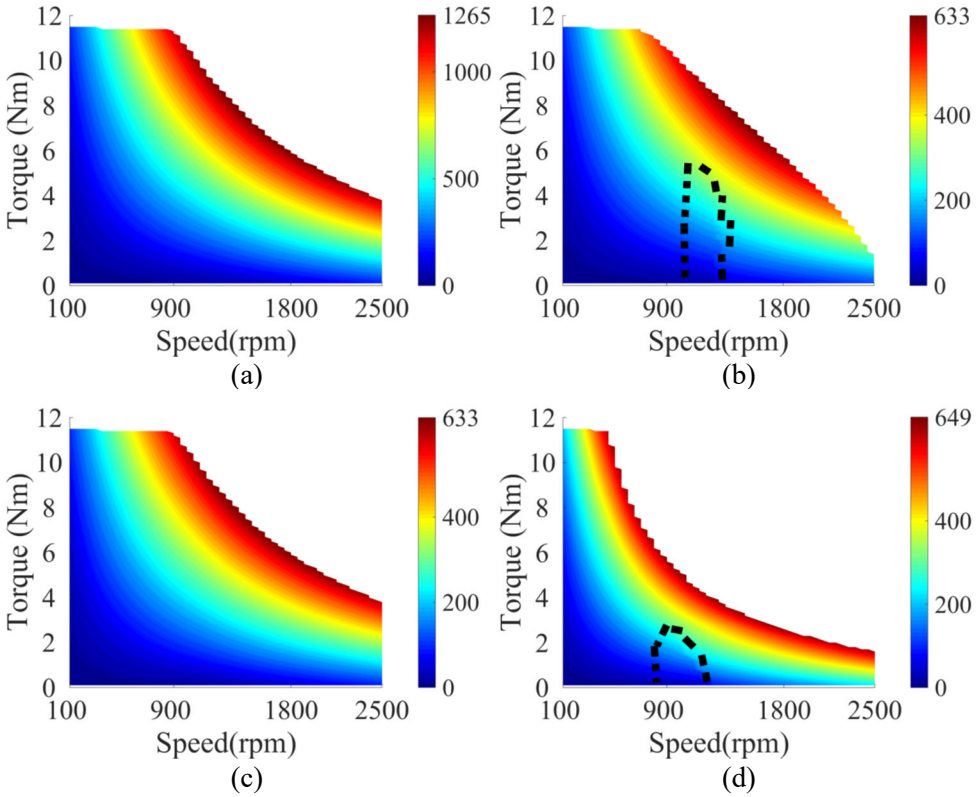

Figure 4.12 Active power contour maps versus speed and torque variations, (a) single inverter, (b) *case 1*, (c) *case 2* and (d) *case 3*

4.6 Summary

The main circuit topologies of dual inverter drives (NIDID and IDID) were introduced and advantages/disadvantages of those topologies were discussed. Three different OW IPMSM drive structures were introduced based on different active/reactive power sharing assumptions. The equations of the controllers and control block diagrams for *case 1*, *case 2* and *case 3* drives were discussed. Both *case 1* and *case 3* drives needed an additional d-q axis current filters to reduce the d-q axis voltage ripples of VSC-1 and VSC-2.

The contour maps of d-axis reference current, efficiency and power factor were presented for all drive cases for comparative study purposes. According to that, all drive configurations can support 11.4 Nm peak torque in the MTPA region. The Single inverter and *case 2* drives showed an identical performance due to having same voltage capability from the utilized VSCs. However,

case 1 drive could not provide the same performance capability due to incompetent power sharing assumptions even though it had enough DC link voltage. The d-axis reference current is limited to -2 A for all dual inverter drives including Single inverter drive. However, it is required to increase up to -4.6~-4.8 A in FW region for maintaining the terminal voltage of the machine at its maximum value.

Conventional Single inverter drive, *case 1* and *case 2* drives can operate with same peak efficiency of 93.5%, but in *case 3,* it has been reduced to 92.6%. However, the considered power sharing assumptions are not valid for all operating in *case 1* and *case 3* drives. In *case 1* and *case 3* the VSC-1 cannot operate at unity power factor at low loading conditions due to limited available DC link voltage. The controllers need to be modified in these regions by avoiding VSC-1 operates at the unity power factor.

In MTPA region, the reactive power absorption of the machine is increased with speed. However, machine starts to produce reactive power in FW region and converters should be capable of absorbing the generated reactive power. In Single inverter drive, the VSC should be capable of providing 1265 W peak power. But in *case 2*, it is sufficient to have 633 W peak power capability for each converter. However, in *case 3*, VSC-1 is the only available active power source and it should be capable to provide 647 W peak power. There is no active power exchange between machine and VSC-2.

Chapter 5

Experimental Verification

The predicted performance and capability of the OW IPMSM analysed in Chapter 3 and Chapter 4 are verified by experimental tests using a built IPMSM. The details of components of the experimental test rig are introduced. The voltages and current profiles of all drives are shown in experiments and in the related operating points. The actual performance capabilities are assessed by tests for conventional single inverter drive while experimental tests are extended to three dual inverter drive cases discussed in Chapter 4 as well. The d- and q-axis current trajectories are found in the experiments for peak power capability of the machine and are compared with the simulations of each drive structure. Assessment of losses is done using experimental data and the experimental efficiency of the machine in maximum power capability in both single inverter and dual inverter drives is compared with the simulation analysis.

5.1 Dual inverter Open Winding IPMSM Test Rig

A full test rig, shown in Figure 5.1, is prepared to conduct experimental analysis.

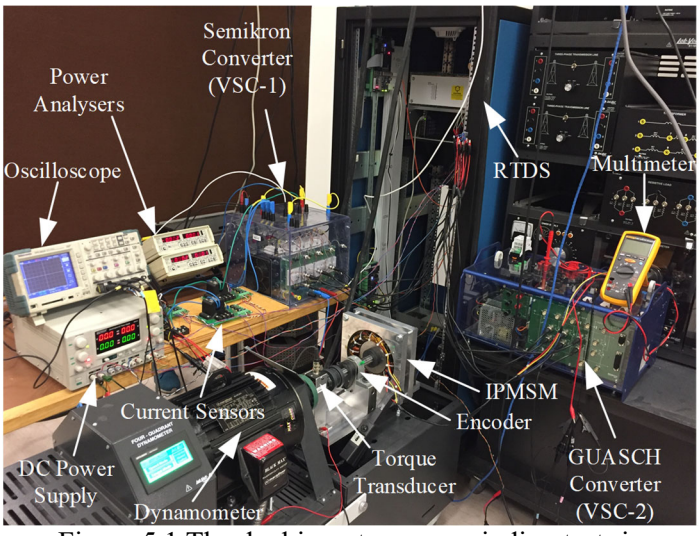

Figure 5.1 The dual inverter open winding test rig

Two three-phase converters are used to provide the Pulse Width Modulated (PWM) signals to the machine's phases in open winding drive configurations. In the single inverter drive case, only VSC-1 is used. The DC link voltage of each converter is supported by a three-phase rectifier included in the corresponding converter and the DC voltage level may be adjusted by a three-phase variac between the grid supply and the rectifier's input.

All controllers are executed in Real Time Digital Simulation (RTDS) using two Freescale MC7448 RISC processors. The control components are built in RSCAD software, which is provided by RTDS Technologies and uploaded into RTDS to run the program.

The developed torque of the machine is adjusted by a Lab-Volt 8540-00 four quadrant dynamometer. It is capable of providing peak power 5 kW with maximum 48 Nm peak torque. The applied torque on the motor shaft is measured using a Futek 20 Nm torque transducer. The rotor position and speed are measured by US Digital 1000 Cycles Per Revolution (CPR) incremental encoder.

The three-phase currents are monitored using LEM LT 100-S current transducers, which have a 1:1000 ratio. An additional instrumental amplifier circuit is used with current transducers to achieve infinite output impedance at measurement side and increases the gain of the transducers to 1:5. The input active power of the machine is determined by VALHALLA 2101 digital power analysers for efficiency calculations.

A Tektronix TPS 2024 oscilloscope is used to monitor currents and voltages and its Fast Fourier Transform (FFT) feature is used to make sure the fundamental component of drawn current is always within the allowed range.

5.2 Voltages and Current Profiles of Drive Cases

The machine is controlled using FOC in MTPA and FW regions. The maximum available DC link voltage in the laboratory is 340 V in the loaded conditions; however, DC link voltage of the single inverter is assumed to be 360 V in simulation analysis. Thus, Space Vector Modulation (SVM) technique is used to operate the machine in single inverter drive in experiments due to the limited available DC link voltage in laboratory. For simplicity, the Sinusoidal PWM (SPWM) technique is used in all dual inverter drives as an enough DC voltage is available to test the machine in open winding drive configurations. The line-line voltage of VSCs and phase current of all drive cases at their corresponding maximum loading conditions are illustrated in Figure 5.2.

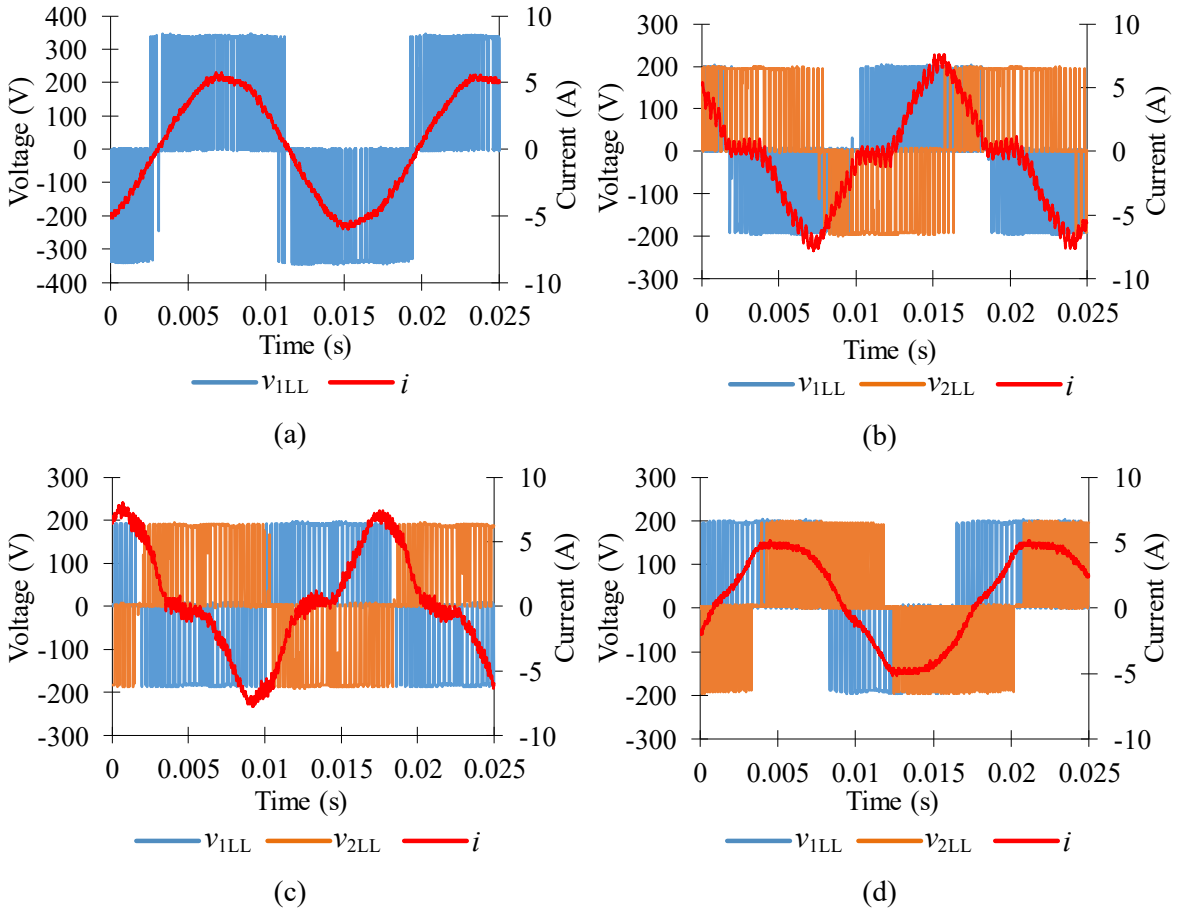

Figure 5.2 Voltage and current profiles of drives for maximum loading at 900 rpm, (a) single inverter, (b) *case 1*, (c) *case 2* and (d) *case 3*

As seen in Figure 5.2, peak to peak current in single inverter, *case 1*, *case 2*, and *case 3* are 11.6 A, 15.2 A, 14 A and 10.4 A, respectively. The current profile of the single inverter drive is very similar to a pure sinusoidal current. However, Figure 5.2(b) and Figure 5.2(c) show a noticeable harmonic distortion in the line current due to the circulating zero sequence current. The normalized current harmonic spectra of each drive structure in its corresponding maximum developed torque are shown in Figure 5.4.

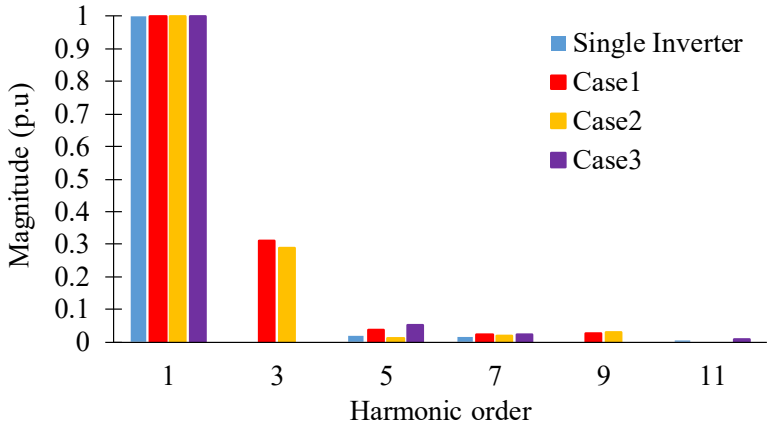

Figure 5.3 Harmonic Spectrum of all drives at 900 rpm for peak loading

According to Figure 5.3, *case 1* and *case 2* show a current THD of 34.1% and 29.1%, respectively, as the phase currents in these cases possess nearly 0.3 pu third-order harmonic content. On the other hand, the current THD of single inverter and *case 3* drives are limited to only 2.6% and 5.6%, respectively. The phase currents of single inverter and *case 3* drives contain odd harmonics without having high amplitude third order harmonics.

Figure 5.2(a) illustrates that the phase current lags the voltage in single inverter drive at the considered operating point. As seen in Figure 5.2(b), phase current lags line voltage of VSC-1 by 30 degree which implies that VSC-1 operates at unity power factor , Figure 5.2(b), Figure 5.2(c) and Figure 5.2(d) show "i lags v_1" and "i leads v_2" in all dual inverter cases for the considered operating points. Figure 5.2(c) confirms that voltages v_1 and v_2 are exactly opposite each other,

i.e., 180 degrees of phase shift. In other words, it satisfies the power sharing assumptions discussed in Section 4.3. The capacitor voltage variation of VSC-2 at the machine starting time for *case 3* is shown in Figure 5.4.

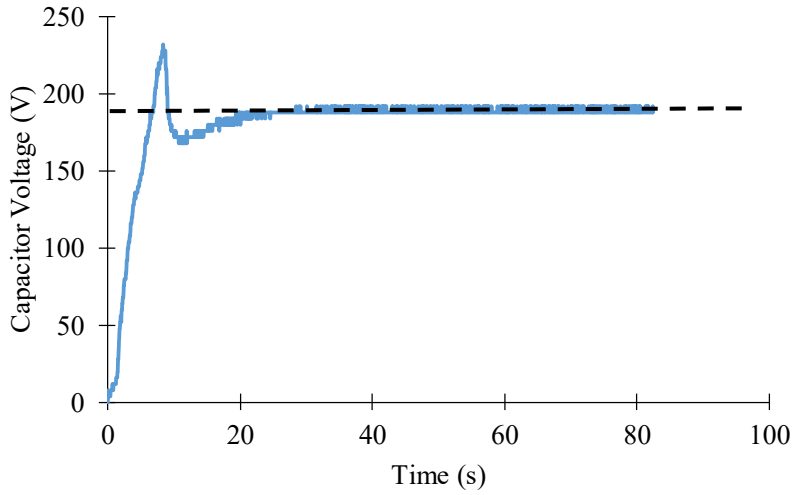

Figure 5.4 Capacitor voltage variation of VSC-2 at starting

As seen in Figure 5.4, the capacitor voltage is under control and the utilized PI controller is capable of keeping the capacitor voltage at the desired value of 180 V by controlling the power flow between machine and VSC-2. According to the developed controller, capacitor voltage shows 27% overshoot during its charging procedure and it takes 20 s for the capacitor voltage to settle on its desired reference value.

5.3 Experimental Validations for Maximum Capability

In this section, maximum developed torque capability of the machine in different drive configurations is evaluated using experimental analysis. As seen in Figure 5.5, a promising agreement between simulations and experimental analysis is seen for the developed torques of the machine in various drive configurations. In MTPA region, the developed experimental torque is at most 4.7% below the simulation analysis, while in FW regions the discrepancies between simulations and experiments may go even below 3.9%. The simulations and experiments are

conducted even in low torque regions and it is shown that in *case 1* and *case 3* drives the defined active and reactive power sharing assumptions should be modified as VSC-2 can no longer be the only source of reactive power to the machine and VSC-1 should also contribute in some part of the required reactive power. Corresponding regions have been highlighted in the torque versus speed profiles in Figure 5.5 for further clarity.

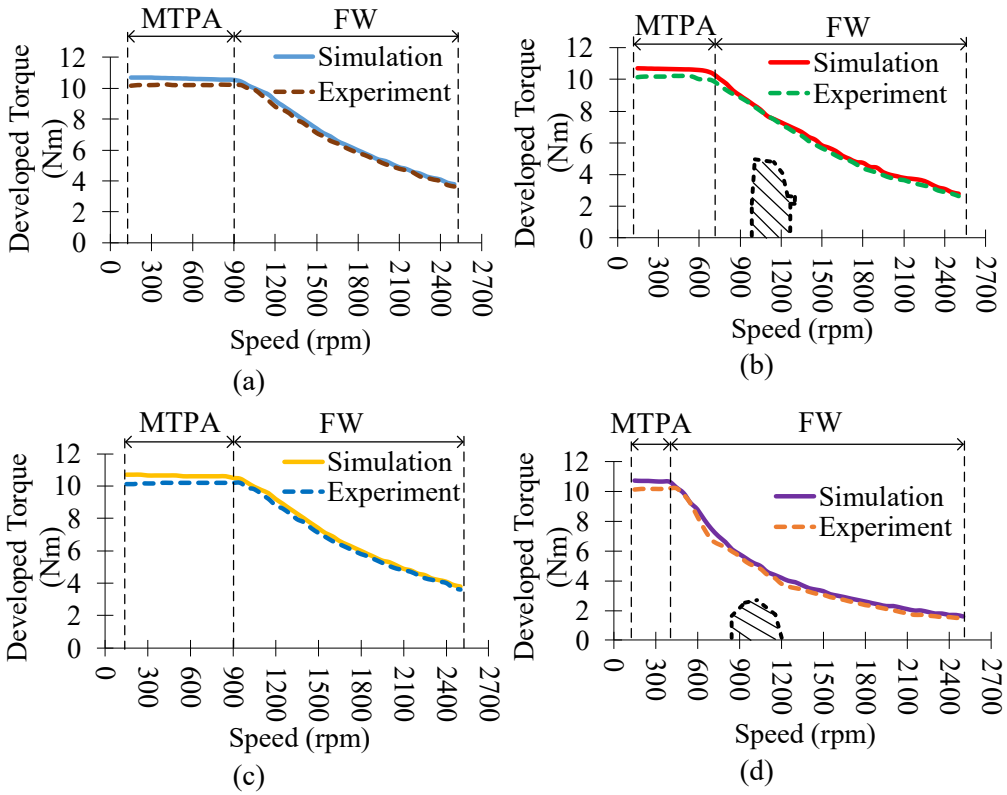

Figure 5.5 Comparison of maximum develop torque capability, (a) s*ingle inverter*, (b) *case 1*, (c) *case 2* and (d) *case 3*

As seen, single inverter and *case 2* drives can support an identical developed torque capability in wide speed range and no control modification is required in any operating points of these drives. The minimum torque capability in 2500 rpm belongs to *case 3* with the experimental developed torque of 1.7 Nm. while the developed torque of single inverter, *case 2*, and *case 1* drives are above 3.7 Nm and 2.7 Nm in this operating speed, respectively.

Figure 5.6 shows the trajectories of d- and q-axis reference current for maximum developed torque capability in simulations and experiments.

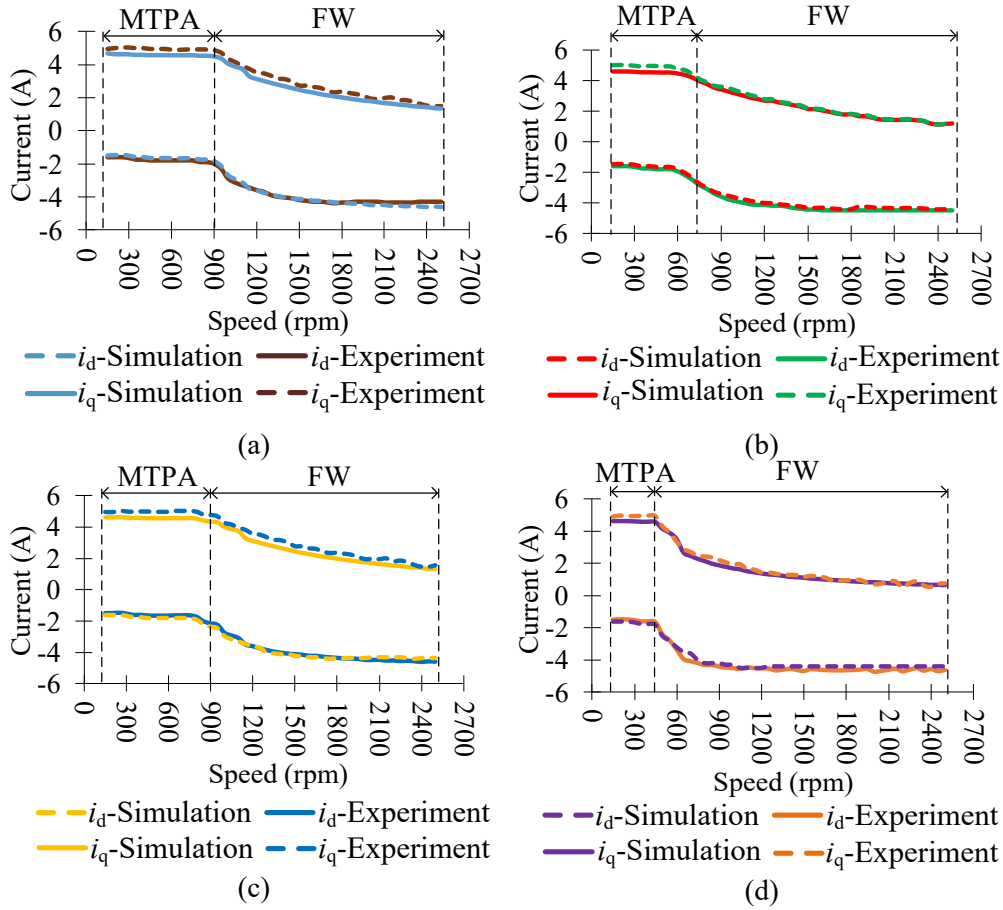

Figure 5.6 Comparison of d- and q-axis current trajectories for peak capability

According to Figure 5.6, the obtained d-axis reference current from the simulation analysis are fairly aligned with the experimental d-axis reference current which confirms that the simulated d-axis reference current is a reliable input for the machine's experimental control in a wide speed range in different drive configurations. A discrepancy of 3% to 5% is seen between the q-axis currents in simulations and experimental results of *case 1* and *case 3* drives in a wide speed range, while this discrepancy is 3% to 6% larger for the single inverter and *case 2* drives.

5.4 Experimental Validations of the Controllers

The voltage controllers of VSC-1 and VSC-2 can be verified by analysing the magnitudes and phase angles of d- and q-axis voltage and current profiles. The phase angle of voltage or current with respect to positive side of the q-axis can be calculated in d-q reference frame as follows.

$$phase\ angle = tan^{-1}\left(\frac{|d-axis\ component|}{q-axis\ component}\right) \tag{5.1}$$

The d- and q-axis currents for all drive cases at base speed and in the maximum corresponding loading conditions are illustrated in Figure 5.7.

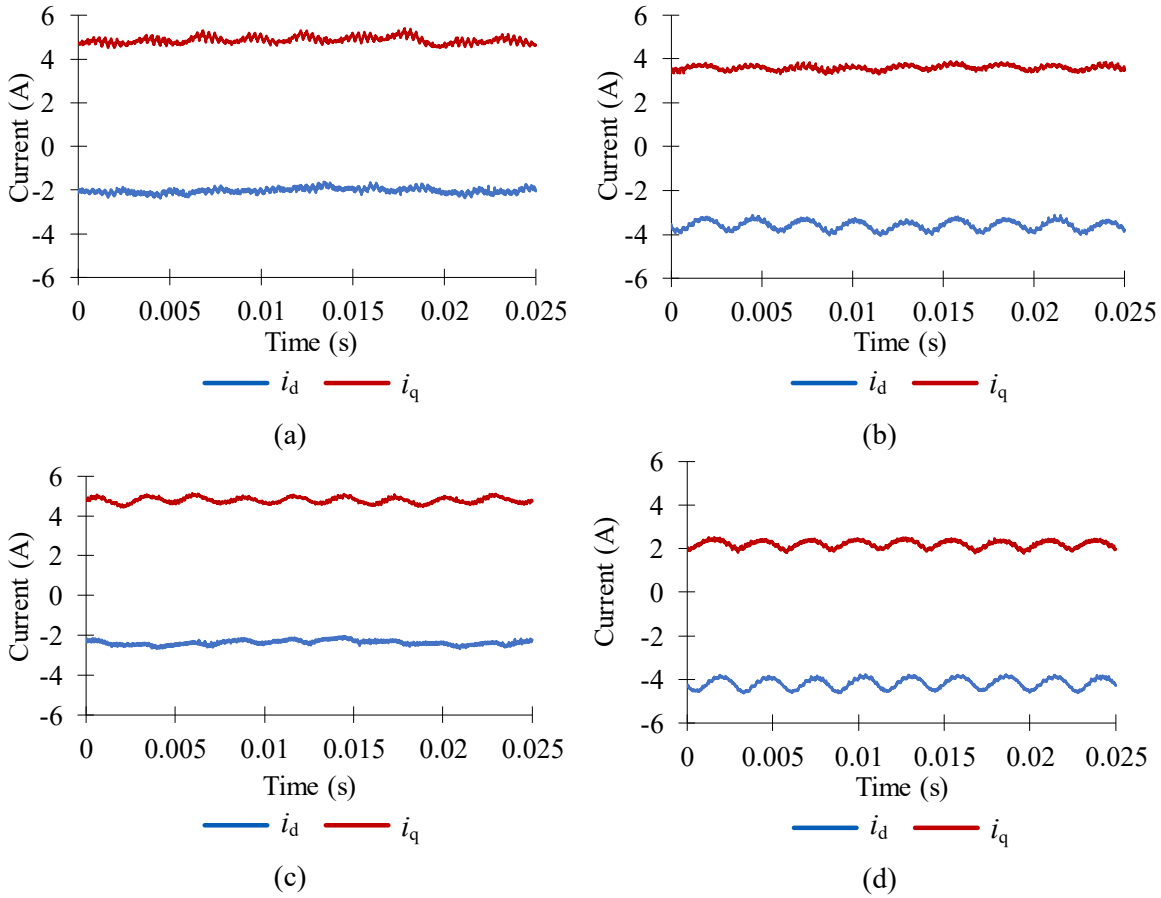

Figure 5.7 d- and q-axis currents of drive cases at maximum corresponding developed capabilities in 900 rpm, (a) *single inverter*, (b) *case 1*, (c) *case 2* and (d) *case 3*

According to Figure 5.7, the average d-axis currents of *single inverter, case 1, case 2* and *case 3* are -2 A, -3.6 A, -2.35 A and -4.2 A respectively, and the average q-axis currents are 4.88 A, 3.6 A, 4.77 A and 2.2 A, respectively. The d- and q-axis currents of single inverter and *case 2* drives are nearly same, because both drives are capable of providing the same maximum developed torque of 10. 2 Nm at 900 rpm. However, larger d-axis current in *case 1* and *case 2* are required to make the air gap field weaker due to limited available DC link voltage. Correspondingly, the q-axis current is smaller in *case 1* and *case 2* compared to other two cases, because of lower developed torque in this operating speed. The d- and q-axis voltages of VSCs in similar operating points are shown for all drive cases in Figure 5.8.

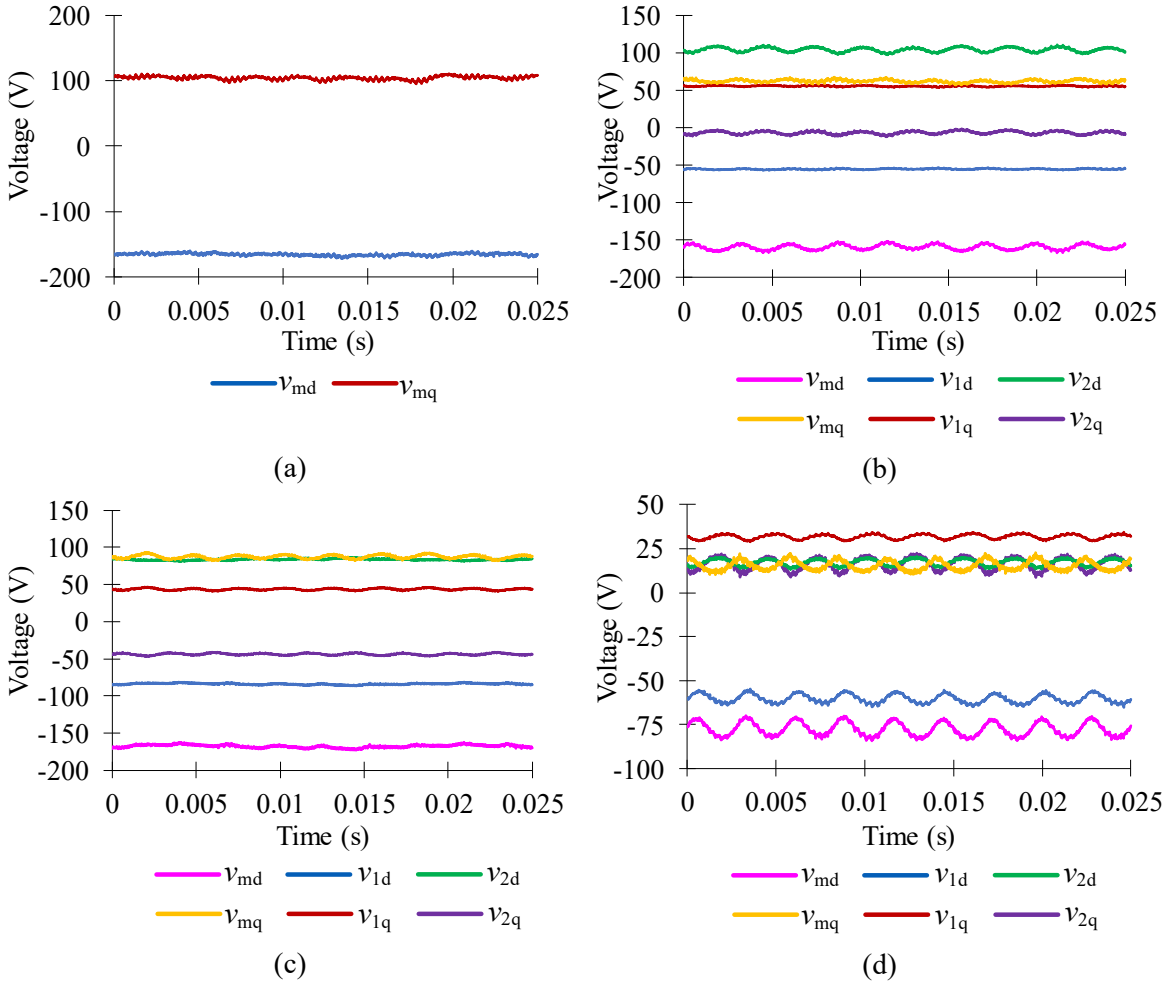

Figure 5.8 d- and q-axis voltages of drive cases in maximum capability at 900 rpm, (a) *single inverter*, (b) *case 1*, (c) *case 2* and (d) *case 3*

As seen in Figure 5.8, all d- and q-axis voltage components satisfy KVL as expected in (4.2) and (4.3). Figure 5.8(b) gives v_{1d}=-55.24 V and v_{1q}= 55.35 V and Figure 5.7(b) gives i_d=-3.6 A and i_q=3.6 A, which show 45° voltage and current angles calculated by (5.1). Hence, it verifies that VSC-1 operates at unity power factor in *case 1* drive. According to Figure 5.8 (c) v_{md}=-167.4 V, v_{1d}=-83.7 V, v_{2d}=83.7 V, v_{mq}= 87.37 V, v_{1q}=43.7 V and v_{2q}=-43.7 V, which satisfies (4.8) and (4.9) for *case 2*. In other words, both active and reactive powers are identically shared between VSC-1 and VSC-2. In *case 3*, the average values of the d-q voltage components for VSC-1 and VSC-2 are equal to v_{1d}=-60.4 V, v_{2d}=17.25 V, v_{1q}=31.85 V, and v_{2q}=16.34 V confirmed by Figure 5.8(d). The average values of d-q current components of i_d=-4.2 A and i_q=2.2 A are illustrated by Figure 5.7(d). Accordingly, the phase angles of voltage vector of VSC-1 and phase current can be calculated as 62.2° using (5.1). Therefore, it validates that the VSC-1 operates at unity power factor in *case 3*. However, the phase angle difference between v_1 and v_2 can be calculated as 108.85°, which states that these two voltages are not exactly perpendicular to each other as was expected in simulation analysis. This issue happens since there is always a small active power exchange between VSC-2 and machine to maintain the voltage of the capacitor at the desired reference value.

5.5 Loss Analysis and Efficiency Evaluation

The copper losses at each operating point of the machine can be estimated using (3.9). The stator per phase DC resistance (R_s) of the built machine is measured as 2.3 Ω. The fundamental component of phase current and R_s is used to calculate the DC copper losses of machine in simulations and experiments. The other losses that take into account core, solid, mechanical and stray losses can be evaluated as follows.

$$Other\,Losses = (P_{core} + P_{mech} + P_{solid} + P_{stray}) = P_m - P_{out} - P_{cu} \tag{5.2}$$

$$Total\ Losses = P_{cu} + P_{core} + P_{mech} + P_{solid} + P_{stray} = P_m - P_{out} \tag{5.3}$$

Figure 5.9 illustrates the total loss (copper loss + other losses) variation in various drive configurations.

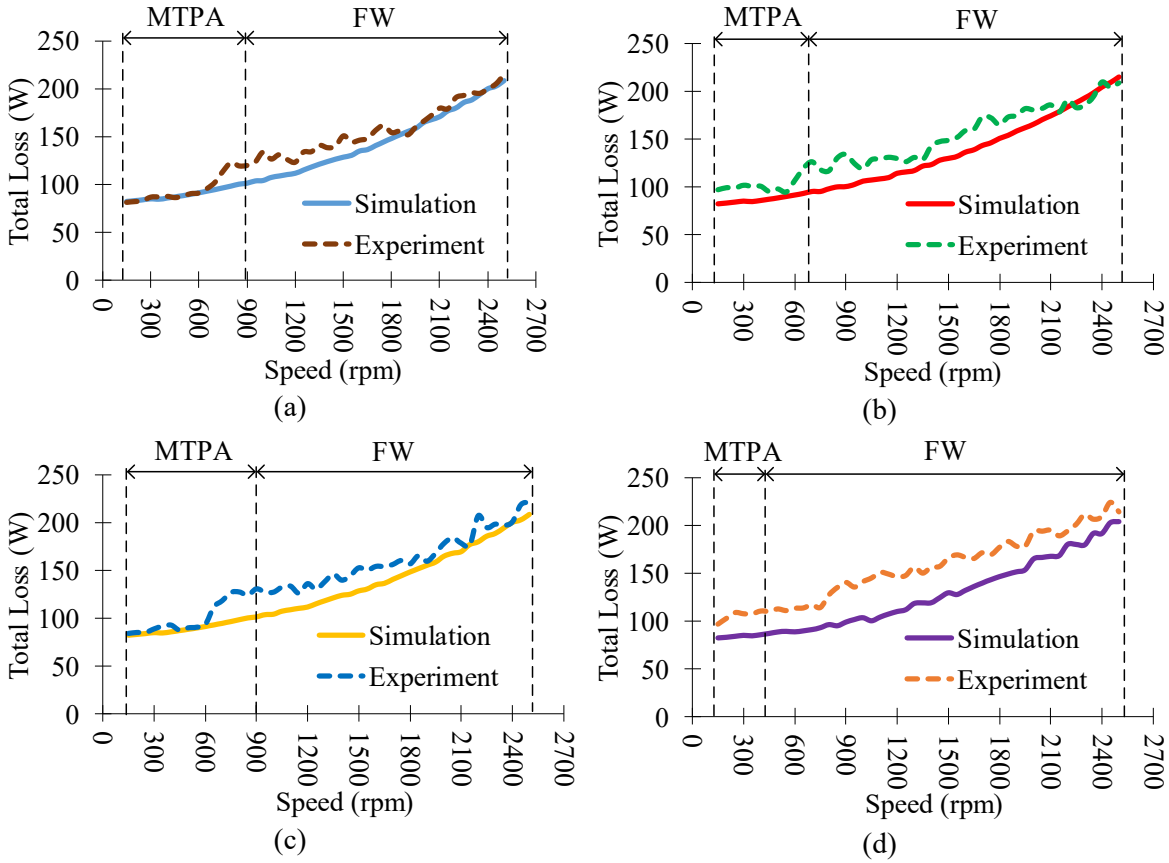

Figure 5.9 Variation of total losses for drives at maximum loading, (a) s*ingle inverter*, (b) c*ase 1*, (c) *case 2* and (d) *case 3*

Generally, the total losses of all drives may vary between 82 W-220 W, in simulations and experiments. In *single inverter* and *case 2* drives, the predicted and experimental total losses are almost similar up to 600 rpm. However, the experimental total losses in those two cases are higher between 600 rpm-1800 rpm. In *case 1*, experimental total losses are always higher than predicted losses up to 2100 rpm. In simulation analysis, the lowest total loss is shown for *case 3*. In experiments, *case 3* shows the largest total losses, mainly because the floating capacitor losses are completely ignored in the prediction.

The variation of the copper losses at the maximum possible power versus speed in both simulations and experiments is shown in Figure 5.10.

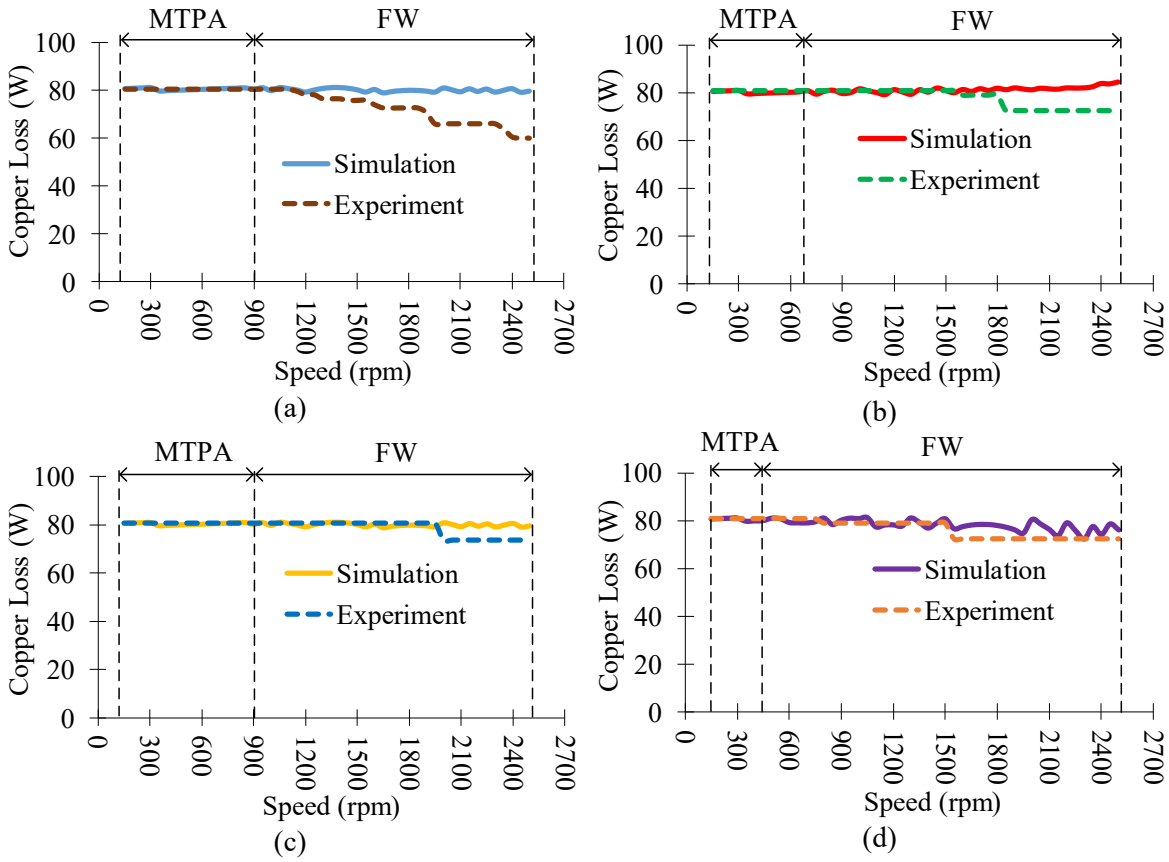

Figure 5.10 Copper loss variation of drives at maximum loading, (a) s*ingle inverter*, (b) *case 1*, (c) *case 2* and (d) *case 3*

As seen in Figure 5.10, copper losses in the simulation are almost fixed at 80 W for all speeds as the phase resistance and current peak are both set to be fixed values in *single inverter, case 1* and *case 2*. There are some fluctuations in the copper losses values in *case 3* in its corresponding FW region. This happens due to the variations of output power in FW region because of a larger torque drop. In MTPA region, it is expected to see almost the same copper losses in experiments for all drive arrangements. This happens because the experimental peak current is kept at the same value as in simulations for MTPA region. However, the copper losses of the machine in *single inverter*, *case 1*, *case 2* and *case 3* drives can even drop to 60 W, 72 W, 78 W and 72 W respectively

at 2500 rpm. Because the peak current is required to be reduced in FW region by lowering the machine's loading to maintain the terminal voltage at the desired level.

The variation of other remaining losses versus speed at maximum developed torque is shown in Figure 5..

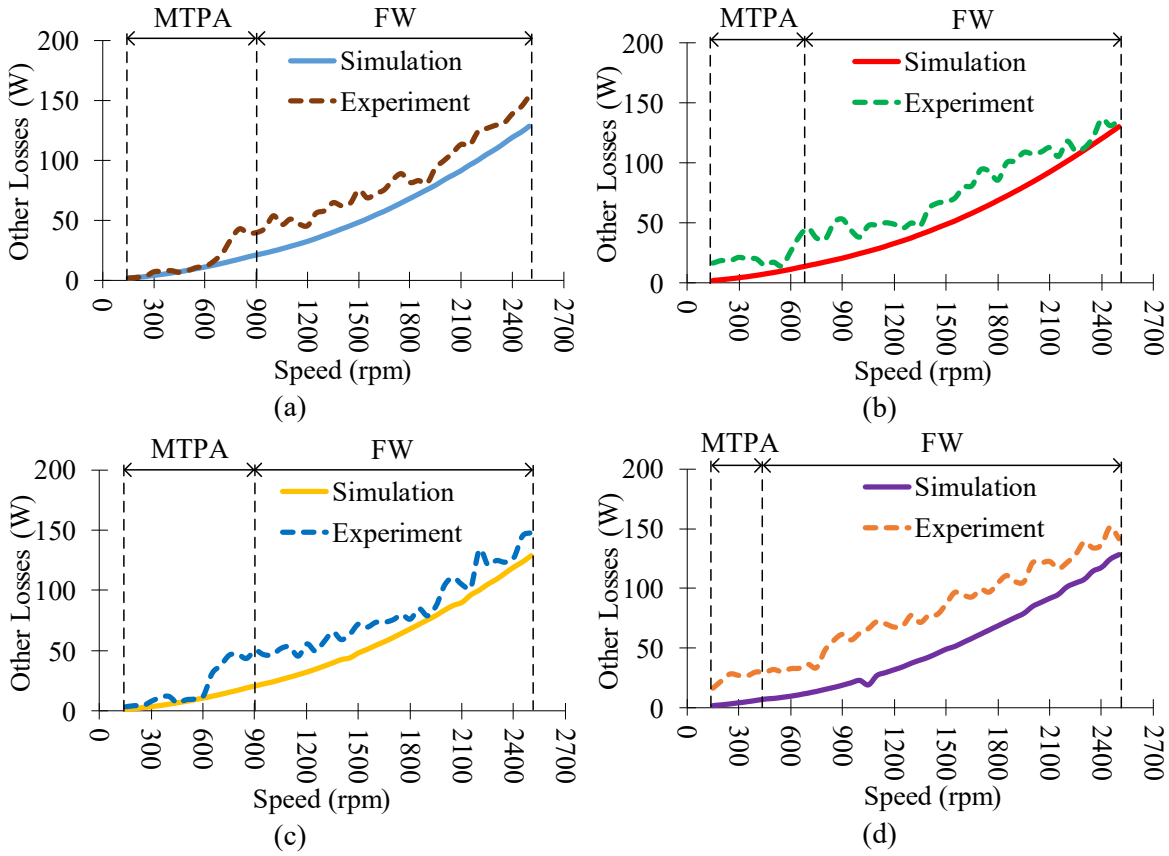

Figure 5.11 Variation of other losses for drives at maximum loading, (a) s*ingle inverter*, (b) *case 1*, (c) *case 2* and (d) *case 3*

According to Figure 5., other losses increase with speed because core, solid and mechanical losses are the function of frequency. The simulated losses are always below the experiments since inverter losses, harmonic losses, and other stray losses are not considered in the simulation analysis. The experimental losses of the machine are always below 50 W in MTPA region for all drives. At the maximum possible speed, other losses of the machine in single inverter, *case 1*, *case*

2 and *case 3* drives can be increased up to 154 W, 135 W, 147 W and 141 W respectively at 2500 rpm in tests.

The developed torque of the machine in experiments is measured using a torque transducer and mechanical speed is given by the incremental encoder. Hence, output power of the machine in experiments can be assessed as follows.

$$P_{\text{out}} = T_{\text{dev}}\omega_{\text{mech}} \tag{5.4}$$

The input power of the machine in experiments are monitored using digital power analysers. Therefore, experimental efficiencies of all drive can be estimated using following equation.

$$Eff\,(\%) = \frac{P_{\text{out}}}{P_{\text{m}}} \times 100 \tag{5.5}$$

The efficiency variation taking into account the total losses of each drive structure is shown in Figure 5..

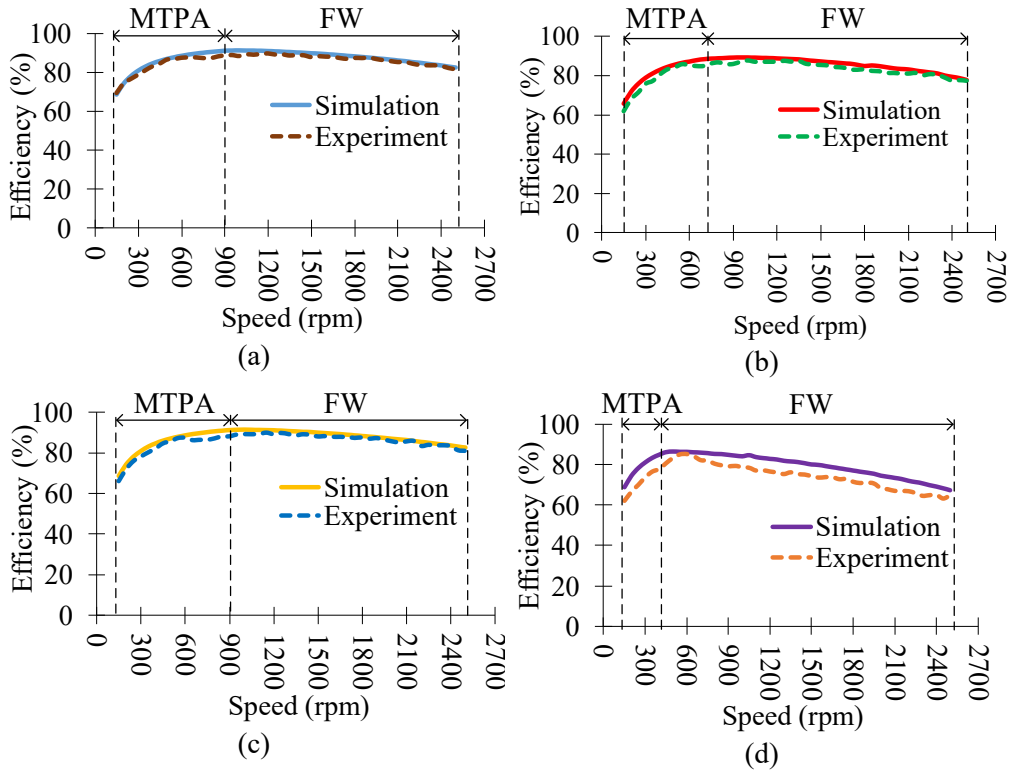

Figure 5.9 Comparison of efficiency (a) *single inverter*, (b) *case 1*, (c) *case 2* and (d) *case 3*

According to the simulations, it is predicted to have a similar 91.5% peak efficiency for *single inverter*, *case 1* and *case 2* while the predicted peak efficiency for *case 3* is 86.4%. However, *single inverter*, *case 1*, *case 2* and *case 3* drives can operate at 90%, 88%, 89.8% and 85.2% peak efficiencies in experiments. There are small discrepancies between predicted experimental efficiency values for single inverter, *case 1* and *case 2* drives because of (i) the non-ideal magnetic properties of the actual laminations and magnets compared to what is used in the simulations, and (ii) small losses that are ignored in simulation analysis, including converter and stray losses. In addition, the efficiency discrepancy is larger in *case 3* drive due to the neglected active power exchange for the VSC-2 in simulation analysis.

According to the reported experimental analysis, the maximum developed torque, d- and q-axis reference currents and voltages, losses and efficiency variations are in a well agreement with the expected results verifying the accuracy of analysis and confirm the reliability of the thesis contributions.

5.6 Summary

The simulations and experimental results of different single inverter and dual inverter drives were compared for the maximum developed torque capability of an IPMSM. The voltages and current profiles were used to validate the accurate operation of each defined corresponding controller. The losses of the machine were separately analysed for corresponding drive structures and efficiencies of the machine were compared both in single inverter and dual inverter drive cases using predicted and experimental values in MTPA and FW regions.

The experimental performance capability of the machine showed a close agreement with the predicted performance. Although the experimental peak torque capability for all drives in MTPA region showed a 4.7% difference compared to the simulation results, this discrepancy dropped to

even below 3.9% in FW region. The experimental d-axis reference current trajectories also showed a promising agreement with predicted results, however there was about 6% difference for the simulated versus experimental q-axis reference currents.

The phase current of *case 1* and *case 2* drives showed a higher THD value due to the existing higher third order harmonics. However, there were no third-order harmonics in phase currents of *single inverter* and *case 2* drives, causing the current THDs of these drives to be around 2% to 6%.

The machine showed the same experimental and predicted copper losses for all drive configurations in MTPA region while the copper losses started to drop in the FW region for the conducted tests. However, other losses including core, solid, friction and windage, bearing and stray losses were increasing with speed in both simulations and experiments. The experimental total and other losses always showed higher values than the predicted total and other losses, however the efficiency profiles of the machine in various drive configurations could satisfy the prediction in a wide speed range. There were some small discrepancies between the tests and simulation results due to non-ideal properties of the fabricated machine and unavoidable additional converter and stray losses associated in the experiments.

Chapter 6

Contributions, Conclusions, and Future Work

The main concluding remarks, contributions, and suggestions for future work are described in this chapter.

6.1 Conclusions and Contributions

The main objective of this thesis was to predict and experimentally verify the performance capability of an OW IPMSM drive, considering the effect of machine's saturation, magnetic losses, and mechanical losses in MTPA and FW regions. In addition to that, the machine's performance capability was analysed for conventional single inverter drive in comparison with dual inverter OW IPMSM drives considering different active and reactive power sharing strategies with a limited available DC voltage for the dual inverter drive cases. The conclusions and contributions of each chapter are summarized below.

The main objective of Chapter 2 was to identify the different categories of PMSM machines and to discuss about different advantages/disadvantages of each category. The machine model could be derived in d-q reference frame using ideal conditions (i.e., neglecting the effect of saturation and losses) and it could be extended to analyse the characteristics of MTPA and VCLMT control techniques. The ideal equation for d-axis reference current was derived assuming the ideal operating conditions neglecting saturation and losses.

Chapter 3 concluded that the magnetic saturation is a function of machine's loading, and inductances, saliency ratio, and PM flux linkage may vary accordingly. The FEA was used to capture the variation of core and solid losses which are dependent on the flux distribution of the machine. The core and solid losses are functions of excitation level and frequency of the machine.

In higher speeds, both core and solid losses of the machine can be raised to 5% and 8% of the rated power, respectively. This concludes that it is not reasonable to neglect these losses at higher speed levels during the analysis. The ideal d- and q-axis equations, which were introduced in Chapter 2, were modified by including all non-linearities and losses. A non-linear optimization technique was used to obtain the d-axis reference current trajectory and performance capability of an IPMSM while considering all dynamic behaviours. The developed torque of an IPMSM could be 4.4% lower in the constant torque region and 29% lower at higher speeds when the saturation and losses were taken into account. The effects of the core saturation, electromagnetic losses, and mechanical losses are necessary for an accurate performance prediction of IPMSM.

The concept of OW IPMSM drives was discussed in Chapter 4. Three OW drive structures were analysed based on different active and reactive power sharing assumptions with limited available DC link voltages while considering core saturation, electromagnetic and mechanical losses. The controllers were developed using voltage decomposition methods based on corresponding active/reactive power sharing assumptions. The control block diagrams were introduced for each drive structure with voltage decomposition equations. The performance capabilities and speed range of each drive cases showed to be directly a function of the active and reactive power sharing assumptions. This analysis verified that identically sharing the active and reactive power between two VSCs in OW IPMSM can support a similar power-speed capability to the single inverter drive with a doubled DC link voltage. It was demonstrated that having enough DC link voltage as in *case 1* is not sufficient to obtain the same power capability as in single inverter drive unless the proper active and reactive power sharing assumptions are defined for the utilized VSCs. In addition, in dual inverter drive *case 1* and *case 3*, the active and reactive power

sharing assumptions were not valid for all operating regions of the drive. Accordingly, the defined controllers for these cases had to be modified for some low torque regions in the FW area.

Chapter 5 described the experimental verifications of the FE simulations of all drives for maximum developed torque capability in MTPA and FW regions. The controllers were implemented in RSCAD according to the assumed active and reactive power sharing assumptions. The correct controller operations were verified by the experimental test results. The simulations of the maximum developed torque capability agreed well with the experimental tests. Also, the experimental d-axis reference current trajectory accurately followed the simulation trajectory and the simulated q-axis reference current showed maximum 6% difference compared to the test results. In experiments, *case 2* drive was capable to provide the same developed torque capability as in *single inverter*. The efficiencies of the dual inverter drives were smaller in experiments compared to the conventional single inverter drive due to additional converter and stray losses in the system.

Overall the dual inverter *case 2* drive could be recommended as an alternative for the single inverter drive supporting a same power capability and speed range with half DC link voltage of the single inverter drive.

6.2 Recommendations for Future Work

The contributions of this thesis can be improved in several ways described as follows.

In Chapter 4, the cross-coupling effect, 3D effects, and current harmonic contents were neglected while capturing the performance capability contour maps. However, Chapter 5 considered these effects for the simulations versus experiments comparison purposes only in the maximum developed torque capability region. Considering the mentioned effects in analysis reported in Chapter 4 could give a more accurate sets of performance indicator contour maps.

In experimental analysis, one of the most important factors is to read the input power of the machine as accurately as possible. The power analysers used in this study showed some reading fluctuations in some operating speeds that made the input power measurements and efficiency evaluation hard. Using a better power analyser with more accurate reading may cause the experimental analysis to be more accurate and the discrepancies between simulations and tests smaller.

The efficiency of the dual inverter drive *case 1* and *case 2* can be improved by minimizing the effect of the third-order harmonic components in the currents that circulate inside the drive circuitry. A new or modified PWM modulation strategy can be introduced to minimize the CMV of the dual inverter drive. The losses of the floating capacitor in *case 3* can be minimized using low-loss capacitors in VSC-2. By doing that, efficiency of the *case 3* can be improved and be closer to the Single inverter drive case. As another solution to make a more accurate prediction, a loss model can be developed for the floating capacitor in *case 3* and it can be included in the analysis to estimate the VSC-2 losses.

6.3 Publications

Two research papers are already presented in highly reputed IEEE international electrical machines conferences and one IEEE journal paper is under review at the time of writing this thesis.

1. Gayan Watthewaduge, Mohammad Sedigh Toulabi, and Shaahin Filizadeh, “Performance prediction of a dual inverter open winding IPMSM drive considering machine’s saturation and losses,” in *Proc*. *IEEE 2018 Int. Conf. on Electr. Machines (ICEM)*, Greece, 2018, pp. 1643-1649.
2. Gayan Watthewaduge, Mohammad Sedigh Toulabi, and Shaahin Filizadeh, “Analysis and control considerations of an open winding IPMSM drive in MTPA and FW regions,” in

Proc. IEEE 2018 Int. Conf. on Electr. Machines and Systems (ICEMS), South Korea, 2018, pp. 137-142.

3. Gayan Watthewaduge, Mohammad Sedigh Toulabi and Shaahin Filizadeh, "Performance analysis and operating limits of a dual inverter open winding IPMSM drive," *IEEE Trans. on Energy Convers.*, submitted (TEC-01053-2018).

References

[1] H. Liu, Z. Gao, W. Wu, L. Chow, and T. Wu., "Design of a high-efficiency permanent magnet synchronous motor and inverter system," in *Proc. IEEE 2015 Annu. Conf. Ind. Electron. Society (IECON)*, 2015, pp. 4996–5001.

[2] J. M. Mun, G. J. Park, S. Seo, D. W. Kim, Y. J. Kim, and S. Y. Jung., "Design characteristics of IPMSM with wide constant power speed range for EV traction," *IEEE Trans. Magn.*, vol. 53, no. 6, pp. 1–4, Jun. 2017.

[3] B. D. S. G. Vidanalage, M. S. Toulabi, and S. Filizadeh, "Multi model design optimization of V-shaped magnet IPM synchronous machines," *IEEE Trans. Energy Convers.*, vol.33, no.3, pp. 1547-1556, Feb. 2018.

[4] M. S. Toulabi, J. Salmon, and A. M. Knight, "Concentrated winding IPM synchronous motor design for wide field weakening applications," *IEEE Trans. Ind. Appl.*, vol. 53, no. 3, pp. 1892–1900, May 2017.

[5] M. S. Toulabi, J. Salmon, and A. M. Knight, "Design, control, and experimental test of an open-winding IPM synchronous motor," *IEEE Trans. Ind. Electron.*, vol. 64, no. 4, pp. 2760–2769, Apr. 2017.

[6] C. Rossi, G. Grandi, and P. Corbelli, "Series hybrid powertrain based on the dual two-level inverter," in *Proc. IEEE 2008 Int. Conf. on Optimization of Electr. and Electron. Equipment*, May. 2008, pp. 277–286.

[7] S. Foti, A. Testa, G. Scelba, *et al*, "An open-end winding motor approach to mitigate the phase voltage distortion on multilevel inverters," *IEEE Trans. Power Electron.*, vol. 33, no. 3, pp. 2404–2416, Mar. 2018.

[8] Y. Wang, T. A. Lipo, and D. Pan, “Half-controlled-converter-fed open-winding permanent magnet synchronous generator for wind applications,” in *Proc. IEEE 2010 Int. Power Electron. and Motion Control Conf. (PEMC)*, Sept. 2010, pp. 123-126.

[9] B. Stumberger, G. Stumberger, D. Dolinar, A. Hamler, and M. Trlep, “Evaluation of saturation and cross-magnetization effects in interior permanent-magnet synchronous motor,” *IEEE Trans. Ind. Appl.*, vol. 39, no. 5, pp. 1264–1271, Sep. 2003.

[10] X. Liu, H. Chen, J. Zhao, and A. Belahcen, “Research on the performances and parameters of interior PMSM used for electric vehicles,” *IEEE Trans. Ind. Electron.*, vol. 63, no. 6, pp. 3533–3545, Jun. 2016.

[11] G. Luo, R. Zhang, Z. Chen, W. Tu, S. Zhang, and R. Kennel, “A novel nonlinear modeling method for permanent-magnet synchronous motors,” *IEEE Trans. Ind. Electron.*, vol. 63, no. 10, pp. 6490–6498, Oct. 2016.

[12] J. Yu, L. Li, J. Zhang, L. Pei, and L. Zhang, “Co-analysis of electromagnetic loss of the high speed PMSM driven by the PWM inverter,” in *Proc*. *IEEE 2016 Int. Conf. on Electr. Machines and Systems (ICEMS)*, 2016, pp. 1–5.

[13] C. Dutta and S. M. Tripathi, “Comparison between conventional and loss d-q model of PMSM,” in *Proc*. *IEEE 2016 Int. Conf. on Emerging Trends in Electr. Electron. Sustainable Energy Systems (ICETEESES)*, 2016, pp. 256–260.

[14] R. Krishnan, *Electric Motor Drives Modelling, Analysis, and Control*, 1st ed. United States of America: Prentice Hall.

[15] Z. Xiaotan, L. Chongjian, L. Yaohua, and W. Chengsheng, “Analysis of a large power PMSM using different control methods,” in *Proc*. *IEEE 2005 Int. Conf. on Electr. Machines and Systems (ICEMS)*, 2005, vol. 1, pp. 416-421.

[16] L. Qinghua, M. A. Jabbar, and A. M. Khambadkone, “Design optimization of interior permanent magnet synchronous motors for wide- speed operation,” in *Proc*. *IEEE 2001 Int. Conf. on Power Electron. and Drive Systems (PEDS)*, 2001, vol. 2, pp. 475–478 vol.2.

[17] X. Liu, H. Chen, J. Zhao and A. Belahcen, "Research on the performances and parameters of interior PMSM used for electric vehicles," *IEEE Trans. Ind. Electron.*, vol. 63, no. 6, pp. 3533-3545, June 2016.

[18] Y. Zhang, W. P. Cao and J. Morrow, "Interior permanent magnet motor parameter and torque ripple analysis for EV traction," in *Proc*. *IEEE 2015 Int. Conf. on Applied Superconductivity and Electromagnetic Devices (ASEMD)*, Shanghai, 2015, pp. 386-387.

[19] L. Chong, R. Dutta and M. F. Rahman, "A comparative study of rotor losses in an IPM with single and double layer concentrated windings," in *Proc*. *IEEE 2010 Int. Conf. on Electr. Machines and Systems (ICEMS)*, Incheon, 2010, pp. 942-946.

[20] P. D. C. Perera, F. Blaabjerg, J. K. Pedersen and P. Thogersen, "A sensorless, stable V/f control method for permanent-magnet synchronous motor drives," *IEEE Trans. Ind. Appl.*, vol. 39, no. 3, pp. 783-791, May-June 2003.

[21] K. Yang, X. Yang, H. Xie, Y. Liu, Y. Zhang and X. Wei, "Stable sensorless V/f and cosφ =1 control for permanent magnet synchronous motor drives," in *Proc*. *IEEE 2014 International Conference on Electrical Machines and Systems (ICEMS)*, Hangzhou, 2014, pp. 3564-3568.

[22] C. Calleja, A. López-de-Heredia, H. Gaztañaga, L. Aldasoro and T. Nieva, "Validation of a modified direct-self-control strategy for PMSM in railway-traction applications," *IEEE Trans. Ind. Electron.*, vol. 63, no. 8, pp. 5143-5155, Aug. 2016.

[23] J. Lara, J. Xu and A. Chandra, "Effects of rotor position error in the performance of field-oriented-controlled PMSM drives for electric vehicle traction applications," *IEEE Trans. Ind. Electron.*, vol. 63, no. 8, pp. 4738-4751, Aug. 2016.

[24] N. Li, Y. Ming, G. Xianguo and X. Dianguo, "A comparative study of model predictive current control and FOC for PMSM," in *Proc. IEEE 2014 International Conference on Electrical Machines and Systems (ICEMS)*, Hangzhou, 2014, pp. 3143-3147.

[25] F. Niu, B. Wang, A. S. Babel, K. Li and E. G. Strangas, "Comparative evaluation of direct torque control strategies for permanent magnet synchronous machines," *IEEE Trans. Power Electron.*, vol. 31, no. 2, pp. 1408-1424, Feb. 2016.

[26] Z. Fu, Y. Du, Y. Sun and H. Zhu, "Unity power factor control of dual permanent magnet synchronous motors fed by five-leg inverter system," in *Proc. IEEE 2015 Int. Conf. on Elect. Machines and Systems (ICEMS)*, Pattaya, 2015, pp. 50-53.

[27] D. Zhu, G. Liu, J. Wang and Q. Chen, "A comparison of two MTPA algorithms for an interior permanent magnet synchronous motor drives," in *Proc. IEEE 2016 Int. Conf. on Electrical Machines and Systems (ICEMS)*, Chiba, 2016, pp. 1-5.

[28] S. Ekanayake, R. Dutta, M. F. Rahman, and D. Xiao, "Deep flux weakening control of a segmented interior permanent magnet synchronous motor with maximum torque per voltage control," in *Proc., IEEE 41st Annual Conf. of Ind. Electron. Society (IECON)*, 2015, pp. 4802–4807.

[29] Y. Zhang, L. Xu, M. Guven, S. Chi, and M. Illindala, "Experimental verification of deep field weakening operation of a 50-kW IPM machine by using single current regulator," *IEEE Trans. Ind. Appl.*, vol. 47, no. 1, pp. 128-133, 2011.

[30] T. M. Jahns, “Flux-weakening regime operation of an interior permanent-magnet synchronous motor drive,” *IEEE Trans. Ind. Appl.*, vol. IA-23, no. 4, pp. 681–689, Jul. 1987.

[31] A. Kumamoto and Y. Hirane, “A semi-closed loop torque control of a buried permanent magnet motor based on a new flux weakening approach,” in *Proc*. *IEEE Conf. Record of the IEEE Ind. Applications Society Annual Meeting,* 1989, pp. 656–661 vol.1.

[32] S. Morimoto, Y. Takeda, T. Hirasa, and K. Taniguchi, “Expansion of operating limits for permanent magnet motor by current vector control considering inverter capacity,” *IEEE Trans. Ind. Appl.*, vol. 26, no. 5, pp. 866–871, Sep. 1990.

[33] Y. Wang, J. Zhu, and Y. Guo, “A comprehensive analytical mathematic model for permanent-magnet synchronous machines incorporating structural and saturation saliencies,” *IEEE Trans. Magn.*, vol. 46, no. 12, pp. 4081–4091, Dec. 2010.

[34] B. Stumberger, G. Stumberger, D. Dolinar, A. Hamler, and M. Trlep, “Evaluation of saturation and cross-magnetization effects in interior permanent-magnet synchronous motor,” *IEEE Trans. Ind. Appl.*, vol. 39, no. 5, pp. 1264–1271, Sep. 2003.

[35] X. Yongxiang, Y. Qingbing, Z. Jibin and W. Hao, "Influence of periodic carrier frequency modulation on stator steel core loss and rotor eddy current loss of permanent magnet synchronous motor," in *Proc*. *IEEE 2014 Int. Conf. on Elect. Machines and Systems (ICEMS)*, Hangzhou, 2014, pp. 2094-2100.

[36] R. Pei, X. Zhang, L. Zeng and S. Li, "Studies of high-frequency iron core loss for synchronous electric machines used in electric vehicles," in *Proc*. *IEEE 2017 Int. Conf. on Elect. Machines and Systems (ICEMS)*, Sydney, NSW, 2017, pp. 1-4.

[37] S. Nalakath, M. Preindl, B. Bilgin, B. Cheng and A. Emadi, "Modeling and analysis of AC resistance of a permanent magnet machine for online estimation purposes," in *Proc. IEEE 2015 Energy Convers. Congress and Exposition (ECCE)*, Montreal, QC, 2015, pp. 314-319.

[38] J. Wang, J. Wu, C. Gan, and Q. Sun, "Comparative study of flux-weakening control methods for PMSM drive over wide speed range," in *Proc. IEEE 2016 Int. Conf. on Electr. Machines and Systems (ICEMS)*, 2016, pp. 1–6.

[39] Y. C. Kwon, S. Kim, and S. K. Sul, "Voltage feedback current control scheme for improved transient performance of permanent magnet synchronous machine drives," *IEEE Trans. Ind. Electron.*, vol. 59, no. 9, pp. 3373–3382, Sep. 2012.

[40] M. N. Uddin, T. S. Radwan, and M. A. Rahman, "Performance of interior permanent magnet motor drive over wide speed range," *IEEE Trans. Energy Convers.*, vol. 17, no. 1, pp. 79–84, Mar. 2002.

[41] C.-T. Pan and S.- Sue, "A linear maximum torque per ampere control for IPMSM drives over full-speed range," *IEEE Trans. Energy Convers.*, vol. 20, no. 2, pp. 359–366, Jun. 2005.

[42] S. J. Underwood and I. Husain, "Online parameter estimation and adaptive control of permanent magnet synchronous machines," *IEEE Trans. Ind. Electron.*, vol. 57, no. 7, pp. 2435-2443, July 2010.

[43] Hyunbae Kim, J. Hartwig and R. D. Lorenz, "Using on-line parameter estimation to improve efficiency of IPM machine drives," in *Proc. IEEE 2002 Annual Power Electron. Specialists Conf.*, Cairns, Qld., Australia, 2002, pp. 815-820 vol.2.

[44] Q. K. Nguyen, M. Petrich and J. Roth-Stielow, "Implementation of the MTPA and MTPV control with online parameter identification for a high speed IPMSM used as traction drive," in *Proc. IEEE 2014 Int. Power Electron. Conf. (IPEC)*, Hiroshima, 2014, pp. 318-323.

[45] G. Schoonhoven and M. N. Uddin, “MTPA- and FW-based robust nonlinear speed control of IPMSM drive using Lyapunov stability criterion,” *IEEE Trans. Ind. Appl.*, vol. 52, no. 5, pp. 4365–4374, Sep. 2016.

[46] S. Y. Jung, J. Hong, and K. Nam, “Current minimizing torque control of the IPMSM using Ferrari's method,” *IEEE Trans. Power Electron.*, vol. 28, no. 12, pp. 5603–5617, Dec. 2013.

[47] Y. Kim and S. Sul, "Torque Control Strategy of an IPMSM Considering the Flux Variation of the Permanent Magnet," in *Proc*. *IEEE 2007 Ind. Appl. Annu. Meeting*, New Orleans, LA, 2007, pp. 1301-1307.

[48] H. Ge, Y. Miao, B. Bilgin, B. Nahid-Mobarakeh and A. Emadi, "Speed range extended maximum torque per ampere control for PM drives considering inverter and motor nonlinearities," *IEEE Trans. Power Electron.*, vol. 32, no. 9, pp. 7151-7159, Sept. 2017

[49] Z. Li and H. Li, “MTPA control of PMSM system considering saturation and cross-coupling,” in *Proc*. *2012 Int. Conf. on Electrical Machines and Systems (ICEMS)*, 2012, pp. 1–5.

[50] Y. Miao, H. Ge, M. Preindl, J. Ye, B. Cheng, and A. Emadi, “MTPA fitting and torque estimation technique based on a new flux-linkage model for interior-permanent-magnet synchronous machines,” *IEEE Trans. Ind. Appl.*, vol. 53, no. 6, pp. 5451–5460, Nov. 2017.

[51] T. Inoue, Y. Inoue, S. Morimoto and M. Sanada, "Mathematical model for MTPA control of permanent-magnet synchronous motor in stator flux linkage synchronous frame," *IEEE Trans. Ind. Appl.*, vol. 51, no. 5, pp. 3620-3628, Sept.-Oct. 2015.

[52] A. Rabiei, T. Thiringer, M. Alatalo and E. A. Grunditz, "Improved maximum-torque-per-ampere algorithm accounting for core saturation, cross-coupling effect, and temperature for

a PMSM intended for vehicular applications," *IEEE Trans. Transport. Electrific.*, vol. 2, no. 2, pp. 150-159, June 2016.

[53] T. Windisch and W. Hofmann, “Loss minimization of an IPMSM drive using pre-calculated optimized current references,” in *Proc. 2011 Annu. Conf. of Ind. Electron. Society (IECON)*, 2011, pp. 4704–4709.

[54] A. Ruf, S. Steentjes, A. Thul and K. Hameyer, "Stator current vector determination under consideration of local iron loss distribution for partial load operation of PMSM," *IEEE Trans. Ind. Appl.*, vol. 52, no. 4, pp. 3005-3012, July-Aug. 2016.

[55] G. Feng, C. Lai and N. C. Kar, "An analytical solution to optimal stator current design for PMSM torque ripple minimization with minimal machine losses," *IEEE Trans. Ind. Electron.*, vol. 64, no. 10, pp. 7655-7665, Oct. 2017.

[56] M. Preindl and S. Bolognani, "Optimal state reference computation with constrained MTPA criterion for PM motor drives," *IEEE Trans. Power Electron.*, vol. 30, no. 8, pp. 4524-4535, Aug. 2015.

[57] A. Boglietti, A. Cavagnino, M. Lazzari and M. Pastorelli, "Predicting iron losses in soft magnetic materials with arbitrary voltage supply: an engineering approach," *IEEE Trans. Magn.*, vol. 39, no. 2, pp. 981-989, March 2003.

[58] D. Pan, F. Liang, Y. Wang, and T. A. Lipo, “Extension of the operating region of an IPM motor utilizing series compensation,” *IEEE Trans. Ind. Appl.*, vol. 50, no. 1, pp. 539–548, Jan. 2014.

[59] R. U. Haque, M. S. Toulabi, A. M. Knight, and J. Salmon, “Wide speed range operation of PMSM using an open winding and a dual inverter drive with a floating bridge,” in *Proc. IEEE Energy Convers. Congress and Exposition (ECCE)*, Sept. 2013, pp. 3784–3791.

[60] D. Sun, Z. Zheng, B. Lin, W. Zhou, and M. Chen, “A hybrid PWM-based field weakening strategy for a hybrid-inverter-driven open-winding PMSM system,” *IEEE Trans. Energy Convers.*, vol. 32, no. 3, pp. 857–865, Sep. 2017.

[61] J. Hong, H. Lee, and K. Nam, “Charging method for the secondary battery in dual inverter drive systems for electric vehicles,” *IEEE Trans. Power Electron.*, vol. 30, no. 2, pp. 909–921, Feb. 2015.

[62] B. A. Welchko, “A double-ended inverter system for the combined propulsion and energy management functions in hybrid vehicles with energy storage,” in *Proc. 2005 IEEE Annu. Conf. of Ind. Electron. Society (IECON)*, Nov. 2005, pp. 1401-1406.

[63] F. Zhang, X. Wang, Q. Liao and C. G. Auth, "Highly integrated bidirectional vehicle-to-grid (V2G) for electric vehicles based on open winding permanent magnet synchronous motor," in *Proc. IEEE 2017 Int. Conf. on Electr. Machines and Systems (ICEMS)*, Sydney, NSW, 2017, pp. 1-4.

[64] M. S. Diab, A. M. Massoud, S. Ahmed, and B. W. Williams, “A dual modular multilevel converter with high-frequency magnetic links between submodules for MV open-end stator winding machine drives,” *IEEE Trans. Power Electron.*, vol. 33, no. 6, pp. 5142–5159, Jun. 2018.

[65] Y. Wang and Z. Deng, “A controllable power distribution strategy for open winding hybrid excitation generator system,” *IEEE Trans. Energy Convers.*, vol. 32, no. 1, pp. 122–136, Mar. 2017.

[66] N. Bodo, M. Jones and E. Levi, "A space vector PWM with common-mode voltage elimination for open-end winding five-phase drives with a single DC supply," *IEEE Trans. Ind. Electron.*, vol. 61, no. 5, pp. 2197-2207, May 2014.

[67] H. Zhan, Z. Zhu and M. Odavic, "Analysis and suppression of zero sequence circulating current in open winding PMSM drives with common DC bus," *IEEE Trans. Ind. Appl.*, vol. 53, no. 4, pp. 3609-3620, July-Aug. 2017.

[68] Q. An, J. Liu, Z. Peng, L. Sun and L. Sun, "Dual-space vector control of open-end winding permanent magnet synchronous motor drive fed by dual inverter," *IEEE Trans. Power Electron.*, vol. 31, no. 12, pp. 8329-8342, Dec. 2016.

[69] X. Zhang and K. Wang, "Current prediction based zero sequence current suppression strategy for the semi controlled open-winding PMSM generation system with a common DC bus," *IEEE Trans. Ind. Electron.*, vol. 65, no. 8, pp. 6066-6076, Aug. 2018.

[70] P. P. Rajeevan, K. Sivakumar, Chintan Patel, et al, “A seven level inverter topology for induction motor drive using two level inverters and floating capacitor for H-bridges” *IEEE Trans. Power Electron.*, vol: 26, no: 6, pp: 1733-1740, 2011.

[71] K. K. Mohapatra, K. Gopakumar, V. T. Somasekhar, and L. Umanand, “A novel modulation scheme for a six-phase induction motor with open end windings” in *Proc*. *IEEE 2002 Annu. Conf. on Ind. Electron. Society (IECON)*, Vol: 1, Pp: 810-815, 2002.

[72] Krushna K. Mohapatra, K. Gopakumar, V. T. Somasekhar, and L. Umanand, “A harmonic elimination and supperposition scheme for open end winding induction motor Drive” *IEEE Trans. Ind. Electron.*, vol: 50, no: 6, pp: 1187-1198, 2003.

[73] V. T. Somasekhar, K. Gopakumar, M. R. Baiju, “Dual two-level inverter scheme for and open-end winding induction motor drive with a single DC power supply and improved DC bus utilization” in *Proc*. *IEEE Proceedings on Electric Power Appl.*, vol: 151, no. 2, pp: 230-238, 2004.

[74] Shivakumar. E, G, Gopakumar. K, Sinha, S. K, et al, “Space vector PWM control of dual inverter fed open end winding induction motor drive” in *Proc*. *IEEE 2006 Annu. Applied Power Electron. Conf. and Exposition (APEC)*, vol: 1, pp: 399-405, 2001.

[75] S. Lakshminarayanan, K. Gopakumar, G. Mondal, et al, “Eighteen-sided polygonal voltage space vector based PWM control for and induction motor drive” *IET, Electric Power Appl.*, vol: 2, no.1, pp: 56-63, 2008.

[76] M. S. Toulabi, J. Salmon and A. M. Knight, "Analysis of a wide speed range open winding IPM with floating bridge," in *Proc*. *IEEE 2015 Int. Symposium on Ind. Electron. (ISIE)*, Buzios, 2015, pp. 1440-1445.

[77] Bin Lin, Dan Sun and Yin Chen, "Research on high-speed operation of hybrid-inverter fed open winding permanent magnet synchronous motor," in *Proc*. *IEEE 2013 Int. Conf. on Elect. Machines and Systems (ICEMS)*, Busan, 2013, pp. 1179-1183.

[78] M. Kwak and S. Sul, "Flux weakening control of an open winding machine with isolated dual inverters," in *Proc*. *IEEE 2007 Ind. Appl. Annu. Meeting*, New Orleans, LA, 2007, pp. 251-255.

[79] J. S. Park and K. Nam, "Dual inverter strategy for high speed operation of HEV permanent magnet synchronous motor," in *Proc*. *Conf. Record of the 2006 IEEE Ind. Appl. Conf. Forty-First IAS Annu. Meeting*, Tampa, FL, 2006, pp. 488-494.

[80] B. Lin and D. Sun, "Analysis on constant power range enhancement in hybrid-inverter open winding PMSM drive system," in *Proc*. *IEEE 2014 Int. Conf. on Electr. Machines and Systems (ICEMS)*, Hangzhou, 2014, pp. 2923-2929.

[81] Y. Wang, T. A. Lipo and D. Pan, "Half-controlled-converter-fed open-winding permanent magnet synchronous generator for wind applications," in *Proc. IEEE 2010 Int. Power Electron. and Motion Control Conf. (EPE-PEMC)*, Ohrid, 2010, pp. T4-123-T4-126.

[82] Z. Zheng, D. Sun and J. Zhu, "Torque ripple suppression of open-winding PMSMs by current injection considering magnetic saturation," in *Proc. IEEE 2016 Vehicle Power and Propulsion Conference (VPPC)*, Hangzhou, 2016, pp. 1-5.

[83] Y. Luo and C. Liu, "Model predictive torque control of an open-end winding PMSM with reduced computation time," in *Proc. IEEE 2017 Int. Conf. on Electr. Machines and Systems (ICEMS)*, Sydney, NSW, 2017, pp. 1-6.